A parametric large-eddy simulation study of wind-farm blockage and gravity waves in conventionally neutral boundary layers

L. Lanzilao^1† and J. Meyers^1

^{1}KU Leuven, Department of Mechanical Engineering, Celestijnenlaan 300 – box 2421, B-3001 Leuven, Belgium

We present a suite of large-eddy simulations of a wind farm operating in conventionally neutral atmospheric boundary layers (CNBLs). A fixed 1.6 GW wind farm is considered for 40 different atmospheric stratification conditions to investigate effects on wind-farm efficiency and blockage, as well as related gravity-wave excitation. A tuned Rayleigh damping layer and a wave-free fringe region method (Lanzilao & Meyers, Bound. Layer Meteor. 186, 2023) are used to avoid spurious excitation of gravity waves, and a domain-size study is included to evaluate and minimize effects of artificial domain blockage. A fully neutral reference case is also considered, to distinguish between a case with hydrodynamic blockage only, and cases that include hydrostatic blockage excited by gravity waves. We discuss in detail the dependence of gravity-wave excitation, flow fields, and wind-farm blockage on capping-inversion height, strength and free-atmosphere lapse rate. In all cases, an unfavourable pressure gradient is present in front of the farm, and a favourable pressure gradient in the farm, with hydrostatic contributions arising from gravity waves at least an order of magnitude larger than hydrodynamic effects. Using respectively non-local and wake efficiencies η_{nl} and η_w (Allaerts & Meyers, Bound. Layer Meteor. 166, 2018), we observe a strong negative correlation between unfavourable upstream pressure rise and η_{nl}, and a strong positive correlation between the favourable pressure drop in the farm and η_w. Using a simplified linear gravity-wave model, we formulate a simple scaling for η_{nl}/η_w, which matches reasonably well with the LES results.

Key words: Flow blockage, Atmospheric gravity waves, Wind farm, Large-eddy simulations

1. Introduction

Conventionally neutral boundary layers (CNBLs) often occur in offshore conditions, with air temperatures adapting to the sea-water temperature given a sufficiently large offshore fetch (Csanady 1974; Smedman *et al.* 1997; Lange *et al.* 2004). Such boundary layers are characterized by a neutral stratification, but with a boundary layer height that is often capped by a strong stably stratified inversion layer (the capping inversion) and a stably stratified free atmosphere aloft; conditions that are driven by larger weather-scale circulation patterns. When large wind farms are operated in a CNBL, they may excite gravity waves consisting of two-dimensional interface waves on the capping inversion and

† Email address for correspondence: luca.lanzilao@kuleuven.be

three-dimensional internal waves in the atmosphere above (Smith 2010; Allaerts & Meyers 2017). This can lead to so-called wind-farm blockage, leading to a significant slow-down of wind speeds in front of the farm, and reducing the overall wind-farm efficiency (Allaerts *et al.* 2018; Bleeg *et al.* 2018). With the current and future plans for large offshore wind-farm developments across the world, a better understanding of the interaction of wind farms with CNBLs is necessary.

To date, the number of large-eddy simulation (LES) studies of wind farms operating in conventionally neutral boundary layers (CNBLs) is limited to a handful of cases. This is mainly due to two facts. First, wind-farm simulations in CNBLs require larger numerical domains than simulations that do not consider thermal stratification above the atmospheric boundary layer (ABL), since the farm has a larger footprint in such conditions (Allaerts & Meyers 2017; Maas 2023). Second, the presence of gravity waves requires the use of appropriate methods for inflow and outflow conditions together with non-reflective upper boundary conditions. Only very recently, a first approach was proposed, based on a wave-free fringe-region technique (Lanzilao & Meyers 2023), that does not excite spurious waves at in- and outlet of the simulation domain, while still allowing for a turbulent inflow in large-eddy simulations. In the current work, we use this approach to set-up a large simulation study that focuses on the influence of thermal stratification above the ABL on wind-farm performance and wind-farm blockage. Moreover, we carefully investigate the effect of domain size on possible artificial domain blockage in case of too small computational domains.

A large part of wind-farm–LESs performed in the past decade made use of pressure-driven boundary layers (PDBLs), which refer to ABLs without Coriolis forces, wind veer and free-atmosphere stratification. This simplified description of the atmosphere is reasonable when turbines are located in the surface layer, where the Coriolis force and boundary-layer height effects are negligible. Early PDBL wind-farm simulations were, e.g., performed by Meyers & Meneveau (2010) and Calaf *et al.* (2010), Wu & Porté-Agel (2011), Lu & Porté-Agel (2011), Yang *et al.* (2014*a*) and Yang *et al.* (2014*b*). These early studies were characterized by the assumption of 'infinite' wind farms, using periodic boundary conditions in all directions, allowing for small simulation domains. With the increase in computational resources, semi-finite and finite wind-farm–LESs were performed, with the goal of investigating the flow behaviour also in regions surrounding the farm. Examples of this type of studies are given by Porté-Agel *et al.* (2013), Wu & Porté-Agel (2013), Wu & Porté-Agel (2015), Stevens *et al.* (2014*b*), Stevens *et al.* (2014*a*), Stevens *et al.* (2016), Wu *et al.* (2019), and Stieren & Stevens (2022). We note that many more PDBL simulations have been presented in the past, including those looking at stable or unstable surface-layer stratification. We refer to Porté-Agel *et al.* (2020) for an extensive overview.

With wind turbines growing in size, the assumption that wind farms operate in the inner part of the ABL is more and more questionable. Therefore, Coriolis forces need to be added to the governing equations, giving rise to the Ekman spiral in the ABL. This type of flow, if no (stable) stratification is present in the free atmosphere (nor the surface layer), is defined as a truly neutral boundary layer (TNBL) in the literature. For instance, the simulations in TNBLs performed by Goit & Meyers (2013) and der Laan *et al.* (2015) clearly show the importance of considering the Coriolis force. However, the equilibrium height of the TNBL can be several kilometers high, scaling with the Rossby–Montgomery height. In practice, this situation rarely occurs, as the free atmosphere is usually stratified starting from 0.5 km to 1 km above the ground, damping turbulence and impeding further boundary layer development. The importance of the inversion layer and stable free atmosphere on the flow within the ABL was, e.g., noted by Csanady

(1974) and Zilitinkevich & Esau (2002). Hess (2004) characterized the entrainment of momentum on the boundary layer as a function of the height of the capping inversion using LES and direct numerical simulation (DNS) while Zilitinkevich & Esau (2003, 2005) and Zilitinkevich *et al.* (2007) improved the equilibrium height formulation for the CNBL. More recently, Taylor & Sarkar (2007, 2008) and Pedersen *et al.* (2014) used LESs to investigate how the capping inversion and free-atmosphere stratification modify the temporal evolution of the CNBL profiles.

Shortly after, CNBLs started to be used also in LESs of wind-farm. Churchfield *et al.* (2012) and Archer *et al.* (2013) were among the first to perform wind-farm LES in CNBLs using SOWFA, an OpenFOAM based LES solver. However, both studies mostly focused on wind-farm wakes and turbine–turbine interactions, without reporting on the effects induced by the presence of a capping inversion and a stably-stratified free atmosphere. Abkar & Porté-Agel (2013) and Allaerts & Meyers (2015) investigated the farm performance and the vertical entrainment of kinetic energy in the ABL under various free-atmosphere stratifications adopting an infinite farm (with periodic boundary conditions). Later, Allaerts & Meyers (2017) explored wind-farm operation in CNBLs using a farm with finite length in the streamwise direction. Here, the vertical domain dimension was extended up to 25 km, to allow for a proper Rayleigh damping layer at the top of the domain, since in a semi-finite wind-farm set-up, internal gravity waves can be triggered. They found that the flow divergence induced by the farm pushes upward the inversion layer, generating a cold anomaly which in turn leads pressure feedbacks and a slow-down of the flow in front of the farm. This result was earlier predicted as well by Smith (2010) based on a linear-theory model. Various more recent studies have further investigated this behaviour both using LES (Allaerts *et al.* 2018; Wu & Porté-Agel 2017; Maas & Raasch 2022; Maas 2022, 2023; Lanzilao & Meyers 2022, 2023) and much faster linearized wind-farm flow models (Smith 2022, 2023; Allaerts & Meyers 2019; Devesse *et al.* 2022).

With the field measurement campaign of Bleeg *et al.* (2018), and later Schneemann *et al.* (2021), demonstrating upstream slow-down of the wind speed in the order of $4 \pm 2\,\%$ in operational wind farms, a lot of research has started focusing on investigating wind-farm blockage. A large part of the literature has concentrated on hydrodynamic blockage (i.e. the joined induction of all turbines in the farm) as a root mechanism to explain blockage, using simple analytical models (Branlard & Meyer Forsting 2020; Branlard *et al.* 2020; Centurelli *et al.* 2021; Segalini 2021), numerical simulations (Bleeg & Montavon 2022; Strickland & Stevens 2020, 2022) and wind-tunnel experiments (Medici *et al.* 2011; Segalini & Dahlberg 2019). These studies report reductions in wind speed at turbine-hub height in the order of 1% to 2%. In CNBL simulations, where next to hydrodynamic effects, also hydrostatic effects arising from gravity waves are present, much larger wind-speed reductions in the order of 10% and more have been reported (Allaerts & Meyers 2017; Maas 2022). Although these studies were performed with a semi-infinite farm, Lanzilao & Meyers (2022, 2023) and Maas (2023) noted similar behaviour in fully finite farms. Comparing these results with field measurements is rather difficult. In fact, gravity-wave effects extend over distances of several tens of kilometers, which makes them difficult to detect using traditional lidar systems. However, recently, analysis of Supervisory Control and Data Acquisition (SCADA) data from the Nordsee Ost and Amrumbank West wind farms located in the German Bight area have shown that velocity deficits and flow-blockage effects are strongly influenced by the capping-inversion height (Cañadillas *et al.* 2023). In the current manuscript, we aim to further investigate relations between wind-farm blockage and capping-inversion height, strength, and free lapse rate, using the LES suite that we present.

This manuscript is further structured as follows. The simulation setup is elaborated in Section 2. Thereafter, Section 3 discusses the boundary-layer initialization. Next, the sensitivity of the farm performance to the width and length of the numerical domain is reported in Section 4 while the sensitivity to the atmospheric state is shown in Section 5. Finally, conclusions are drawn in Section 6.

2. Methodology

The governing equations and the LES solver are described in Sections 2.1 and 2.2, respectively. Next, the boundary conditions and the buffer layers adopted to minimize wave reflection are discussed in Section 2.3. Finally, the numerical setup, wind-farm layout and atmospheric states are summarized in Sections 2.4, 2.5 and 2.6, respectively.

2.1. *Governing equations*

In the current study, we make use of the incompressible filtered Navier–Stokes equations coupled with a transport equation for the potential temperature to investigate the flow in and around a large-scale wind farm (Allaerts & Meyers 2017). Such equations read as

$$\frac{\partial \tilde{u}_i}{\partial x_i} = 0, \tag{2.1}$$

$$\frac{\partial \tilde{u}_i}{\partial t} + \frac{\partial}{\partial x_j}\left(\tilde{u}_j \tilde{u}_i\right) = f_c \epsilon_{ij3}\tilde{u}_j + \delta_{i3}g\frac{\tilde{\theta} - \theta_0}{\theta_0} - \frac{\partial \tau_{ij}^{\mathrm{sgs}}}{\partial x_j} - \frac{1}{\rho_0}\frac{\partial \tilde{p}^*}{\partial x_i} - \frac{1}{\rho_0}\frac{\partial p_\infty}{\partial x_i} + f_i^{\mathrm{tot}}, \tag{2.2}$$

$$\frac{\partial \tilde{\theta}}{\partial t} + \frac{\partial}{\partial x_j}\left(\tilde{u}_j \tilde{\theta}\right) = -\frac{\partial q_j^{\mathrm{sgs}}}{\partial x_j}, \tag{2.3}$$

where the horizontal directions are denoted with $i = 1, 2$ while the vertical one is indicated by $i = 3$. Moreover, δ_{ij} denotes the Kronecker delta while ϵ_{ijk} is the Levi-Civita symbol. The filtered velocity and potential temperature fields are noted with $\tilde{u}_i$ and $\tilde{\theta}$, respectively.

The first term on the right-hand side represents the Coriolis force due to planetary rotation, where the frequency $f_c = 2\Omega_E \sin\phi$, with Ω_E the Earth angular velocity and ϕ the Earth latitude. The second component of the angular velocity vector $\Omega_E \cos\phi$ is neglected here since it is negligible when compared to the other terms in the momentum equations (Wyngaard 2010). Thermal buoyancy is taken into account by the second term, where $g = 9.81$ m s^{-2} denotes the gravitational constant and θ_0 is a reference potential temperature. Moreover, we make use of the Boussinesq approximation so that the incompressible continuity equation holds. This assumption has two implications. First, fluctuations in density are related to thermal effects rather than pressure ones, so that acoustic waves are filtered out. Second, all density variations from the background state are neglected except for the buoyancy term. Consequently, the thermodynamic equation has a direct influence only on the vertical momentum equation. This is a valid assumption for our study since the scale of the vertical motions is much smaller than the density scale height, which is typically in the order of 7 km (Spiegel & Veronis 1960; Allaerts 2016). Moreover, Maas (2022) performed two wind-farm–LESs, one with Boussinesq approximation and one with the anelastic assumption. He found nearly identical numerical results at turbine-hub height, with only minor differences several kilometers above the ABL.

The flow is driven across the domain by applying a steady background pressure gradient $\partial p_\infty / \partial x_i$, with $i = 1, 2$. The latter is related to the geostrophic wind G through the

geostrophic balance. The pressure oscillations around p_∞ are denoted with $\tilde{p}^*$. Moreover, the term $f_i^{\text{tot}} = f_i + f_i^{\text{ra}} + f_i^{\text{fr}}$ groups all external forces exerted on the flow. Here, f_i^{ra} and f_i^{fr} represent the body forces applied within the RDL and fringe region, respectively, while f_i denotes the wind-turbine drag force. Finally, the effects of unresolved scales are modelled by the subgrid-scale stress tensor τ_{ij}^{sgs} and the subgrid-scale heat flux q_j^{sgs}. The notations (x_1, x_2, x_3) and (x, y, z), $(\tilde{u}_1, \tilde{u}_2, \tilde{u}_3)$ and $(\tilde{u}, \tilde{v}, \tilde{w})$ and $\tilde{p}^*$ and $\tilde{p}$ are used interchangeably. Moreover, for the sake of simplicity, the tilde will not be used in the rest of the dissertation.

2.2. *Flow solver*

The governing equations (2.1-2.3) are solved using the SP-Wind solver, an in-house software developed over the past 15 years at KU Leuven (Meyers & Sagaut 2007; Calaf *et al.* 2010; Goit & Meyers 2015; Allaerts & Meyers 2017; Munters & Meyers 2018; Allaerts & Meyers 2018; Lanzilao & Meyers 2022, 2023). The solver structure adopted here is mainly based on the version developed and used in Allaerts & Meyers (2017) and Lanzilao & Meyers (2022, 2023). The equations are advanced in time using a classic fourth-order Runge–Kutta scheme with a time step based on a Courant–Friedrichs–Lewy number of 0.4. The streamwise (x) and spanwise (y) directions are discretized with a Fourier pseudo-spectral method. This implies that all linear terms are discretized in the spectral domain while non-linear operations are computed in the physical domain, reducing the cost of convolutions from quadratic to log-linear (Fornberg 1996). Further, the 3/2 dealiasing technique proposed by Canuto *et al.* (1988) is adopted to avoid aliasing error. For the vertical dimension (z), an energy-preserving fourth-order finite difference scheme is adopted (Verstappen & Veldman 2003). The effects of subgrid-scale motions on the resolved flow are taken into account with the stability-dependent Smagorinsky model proposed by Stevens *et al.* (2000) with Smagorinsky coefficient set to $C_s = 0.14$, similarly to previous study performed with SP-Wind. The constant C_s is damped near the wall by using the damping function proposed by Mason & Thomson (1992). Furthermore, continuity is enforced by solving the Poisson equation during every stage of the Runge–Kutta scheme. In regard to the turbine trust force, we model it using a non-rotating actuator disk model (ADM) (Goit & Meyers 2015; Allaerts & Meyers 2015). We refer to Delport (2010) for more details on the discretization of the continuity and momentum equations while the implementation of the thermodynamic equation and SGS model are explained in detail in Allaerts (2016).

2.3. *Boundary conditions*

The effect of the bottom wall on the flow is modelled with classic Monin–Obukhov similarity theory for neutral boundary layers (Moeng 1984). This wall-stress boundary condition is only dependent on the surface roughness z_0, which we assume to be constant. We refer to Allaerts (2016) for further details on the implementation. Periodic boundary conditions are naturally imposed at the streamwise and spanwise sides of the computational domain. At the top of the domain, a rigid-lid condition is used, which implies zero shear stress and vertical velocity and a fixed potential temperature. However, in case of stratified free atmospheres, a rigid-lid condition reflects back gravity waves triggered by the wind-farm drag force. To minimize gravity-wave reflection, we adopt a Rayleigh damping layer (RDL) in the upper part of the domain (Klemp & Lilly 1977; Durran & Klemp 1983; Allaerts & Meyers 2017; Lanzilao & Meyers 2023). This body force dissipates the upward energy transported by gravity waves before it reaches the top of the domain

and it reads as:

$$f_i^{\mathrm{ra}}(\boldsymbol{x}) = -\nu(z)\left(u_i(\boldsymbol{x}) - U_{G,i}\right) \tag{2.4}$$

where $U_{G,1} = G\cos\alpha$, $U_{G,2} = G\sin\alpha$ and $U_{G,3} = 0$ with α the geostrophic wind angle. Moreover, $\nu(z)$ is a one-dimensional function which reads as:

$$\nu(z) = \nu^{\mathrm{ra}}N\left[1 - \cos\left(\frac{\pi}{s^{\mathrm{ra}}}\frac{z - \left(L_z - L_z^{\mathrm{ra}}\right)}{L_z^{\mathrm{ra}}}\right)\right] \tag{2.5}$$

where L_z and L_z^{ra} denote the height of the computational domain and of the RDL, respectively, while $N = \sqrt{g\Gamma/\theta_0}$ represents the Brunt–Väisälä frequency, with Γ the lapse rate in the free atmosphere. Moreover, ν^{ra} controls the force magnitude while s^{ra} regulates the function gradient along the vertical direction. Lanzilao & Meyers (2023) have shown that the quality of the RDL strongly depends on these two tuning parameters, which are carefully tuned with the aim of minimizing gravity-wave reflection – see Section 2.4.

The periodic boundary condition along the streamwise direction recycles back the wind-farm wake. To break the periodicity and impose an inflow condition, we use a fringe technique (Spalart & Watmuff 1993; Lundbladh *et al.* 1999; Nordstrom *et al.* 1999; Stevens *et al.* 2014*b*; Inoue *et al.* 2014; Munters *et al.* 2016; Lanzilao & Meyers 2023). This body force reads as:

$$f_i^{\mathrm{fr}}(\boldsymbol{x}) = -h(x)\left(u_i(\boldsymbol{x}) - u_{\mathrm{prec},i}(\boldsymbol{x})\right),$$

where $u_{\mathrm{prec},i}(\boldsymbol{x})$ denotes the statistically-steady inflow fields provided by a precursor simulation. Moreover, $h(x)$ is a one-dimensional non-negative function which is non-zero only within the fringe region, and is expressed as

$$h(x) = h_{\max}\left[F\left(\frac{x - x_s^h}{\delta_s^h}\right) - F\left(\frac{x - x_e^h}{\delta_e^h} + 1\right)\right]$$

with

$$F(x) = \begin{cases} 0, & \text{if } x \leqslant 0 \\ \dfrac{1}{1 + \exp\left(\dfrac{1}{x-1} + \dfrac{1}{x}\right)}, & \text{if } 0 < x < 1 \\ 1, & \text{if } x \geqslant 1. \end{cases}$$

The parameters x_s^h and x_e^h denote the start and end of the fringe function support while its smoothness is regulated by δ_s^h and δ_e^h. Moreover, $h_{\max}$ denotes the maximum value of the fringe function.

Lanzilao & Meyers (2023) noted that the standard fringe technique triggers spurious gravity waves which propagate through the domain of interest, significantly altering the numerical results. Therefore, in the current study we use the new wave-free fringe-region technique developed by Lanzilao & Meyers (2023). In addition to applying the body force f_i^{fr} described above, this technique also damps the convective term in the vertical momentum equation within the fringe region, multiplying it by the following damping function:

$$d(x,z) = 1 - \left[F\left(\frac{x - x_s^d}{\delta_s^d}\right) - F\left(\frac{x - x_e^d}{\delta_e^d} + 1\right)\right]\mathcal{H}(z - H). \tag{2.6}$$

Here, x_s^d and x_e^d define the start and end of the damping function support while δ_s^d and δ_e^d control the function smoothness. Moreover, H denotes the capping-inversion height

while $\mathcal{H}$ represents a Heaviside function. For more details, we refer to Lanzilao & Meyers (2023) and to Section 2.4 below.

2.4. *Numerical set-up*

The flow solver makes use of two numerical domains concurrently marched in time, i.e. the precursor and main domains. The precursor domain does not contain turbines and is only used for generating a turbulent fully developed statistically steady flow which drives the simulation in the main domain. Similarly to Allaerts & Meyers (2017, 2018), we fix the precursor domain length and width to $L_x^p = L_y^p = 10$ km, with $L_z^p = 3$ km. The wind farm is located in the main domain. The first-row turbine should be far enough from the inflow to properly capture the flow slow down in the farm induction region. Moreover, the last-row turbine should be far enough from the fringe region to minimize spurious effects and to let the farm wake to develop. Similarly, the domain width should be large enough to minimize sidewise blockage and to limit the channelling effects at the farm sides. In section 4, we present an extensive domain sensitivity study. Based on this, we select a domain size of $L_x \times L_y = 50 \times 30$ km^2, with distance between main domain inflow and first-row turbine of $L_{\text{ind}} = 18$ km. This domain size is further used for all simulations performed in Section 5. The vertical domain dimension is dictated by the presence of gravity waves. Following previous studies, we fix the main domain height to $L_z = 25$ km (Allaerts & Meyers 2017, 2018; Lanzilao & Meyers 2022, 2023). This allows us to insert a wide RDL at the top of the domain– see below.

In SP-Wind, the precursor domain width and height should match the ones of the main domain when they are run concurrently. Therefore, we adopt the tiling technique to extend the precursor flow fields in the y-direction from 10 to 30 km (Sanchez Gomez *et al.* 2023). In regard to the z-direction, we extrapolate the flow fields from 3 to 25 km, using a constant geostrophic wind. At these altitudes the flow is laminar and no turbulence needs to be added.

In regard to the grid resolution, we fix $\Delta x = 31.25$ m and $\Delta y = 21.74$ m in the streamwise and spanwise direction, respectively. This leads to $N_x = 1600$ and $N_y = 1380$ grid points for the main domain and to $N_x^p = 320$ and $N_y^p = 460$ points for the precursor domain. A stretched grid is adopted in the vertical direction. The latter is composed of 300 uniformly spaced grid points within the first 1.5 km to capture the strong velocity gradients around the turbine-rotor disk, leading to a grid resolution of $\Delta z = 5$ m. This allows us to obtain a ratio between Δz and the buoyancy length scale $l_b = 1.69\langle\overline{w'w'}\rangle^{0.5} N^{-0.5}$ in the capping inversion and free atmosphere above 2 for the majority of the simulation cases (Otte & Wyngaard 2001; Pedersen *et al.* 2014). Next, a first stretch is applied from 1.5 to 15 km, where 180 points are used. A second one is applied in the last 10 km of the domain, i.e. from 15 to 25 km. In summary, the domain is 25 km high and the vertical grid contains a total of 490 grid points. The combination of spanwise and vertical grid resolution allows us to have a total of 9 and 40 grid points along the turbine-rotor disk width and height, which is in accordance with simulations in the literature (Calaf *et al.* 2010; Wu & Porté-Agel 2011; Allaerts & Meyers 2017). The combination of precursor and main numerical domains leads to a total of approximately 5.2×10^9 DOF. Finally, we also perform 4 simulations on a domain which contains a single turbine. In these cases, the precursor and main domains have equal sizes. Those simulations are used for evaluating the power output of a turbine that operates in isolation, which will serve in Section 5 for scaling some of the results. More information about the single-turbine simulations is reported in Appendix A.

The vertical gravity-wave wavelength derived using gravity-wave linear theory under the hydrostatic assumption is given by $\lambda_z = 2\pi G/N$. According to the free lapse rate
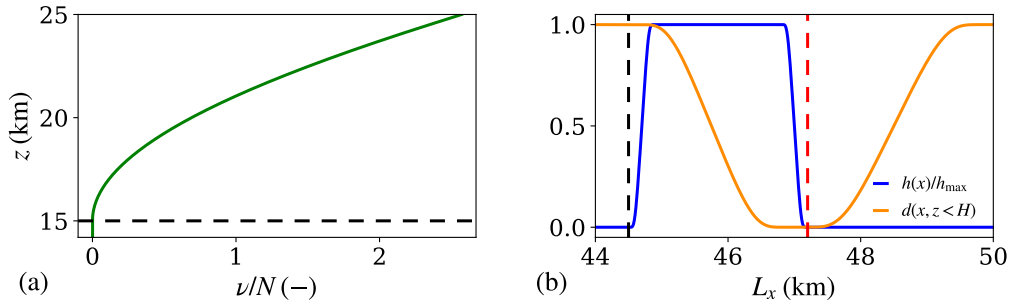
FIGURE 1. (a) Rayleigh function obtained with $\nu^{\mathrm{ra}} = 5.15$ and $s^{\mathrm{ra}} = 3$ values. (b) Fringe and damping functions used with the wave-free fringe-region techniques. The black horizontal and vertical dashed lines denote the start of the RDL and the fringe region while the red vertical dashed line marks the end of the fringe forcing.

values adopted in our study (see Section 2.6), the vertical wavelength varies between 3.8 and 10.7 km. Following Klemp & Lilly (1977), who suggested that the depth of the RDL should be at least in the order of λ_z, we set $L_z^{\mathrm{ra}} = 10$ km. Moreover, we fix $\nu^{\mathrm{ra}} = 5.15$ and $s^{\mathrm{ra}} = 3$. These parameters minimize gravity-wave reflection and are chosen following the procedure detailed in Lanzilao & Meyers (2023). The Rayleigh function is shown in Figure 1(a).

The body force applied within the fringe region should be strong enough to impose the inflow condition without violating the stability constraint imposed by the 4th order Runge–Kutta method (Schlatter *et al.* 2005). We carried out some tests (not shown) and we noted that $h_{\mathrm{max}} = 0.3\,\mathrm{s}^{-1}$ satisfies both constraints. Moreover, we fix the fringe-region length to $L_x^{\mathrm{fr}} = 5.5$ km. Given the wind-farm layout (see Section 2.5), this means that there are gaps of 18 km and 11.65 km upwind and downwind of the farm. Further, we set $x_s^h = L_x - L_x^{\mathrm{fr}}$, $x_e^h = L_x - 2.8$ km and $\delta_s^h = \delta_e^h = 0.4$ km while $x_s^d = x_s^h$, $x_e^d = L_x$, $\delta_s^d = 2.5$ km and $\delta_e^d = 3$ km. Lanzilao & Meyers (2023) have shown that this set of parameters minimize the spurious gravity waves triggered by the fringe forcing. The fringe and damping functions are shown in Figure 1(b).

2.5. *Wind-farm layout*

The wind-farm set-up is inspired by the work of Lanzilao & Meyers (2022, 2023). Hence, we have 16 rows and 10 columns for a total of $N_t = 160$ IEA offshore turbines (Bortolotti *et al.* 2019) with a rated power of $P_{\mathrm{rated}} = 10$ MW arranged in a staggered layout with respect to the main wind direction. The farm is relatively densely spaced with streamwise and spanwise spacings set to $s_x D = s_y D = 5D$, where $D = 198$ m denotes the turbine-rotor diameter. This corresponds to a density of roughly $P_{\mathrm{rated}}/s_x s_y D^2 \approx 10$ MW km^{-2}, which is a relatively dense scenario that is nonetheless considered nowadays in some development areas.

The turbine-hub height measures $z_h = 119$ m while the thrust coefficient is selected from the turbine thrust curve using the undisturbed inflow wind speed at hub height measured in the precursor simulations, which results in $C_T = 0.88$ (Bortolotti *et al.* 2019). The corresponding disk-based thrust coefficient is then $C_T' = 1.94$ (Calaf *et al.* 2010; Meyers & Meneveau 2010). Moreover, a simple yaw controller is implemented to keep all turbine-rotor disks perpendicular to the incident wind flow measured one rotor diameter upstream.

The farm has length and width of $L_x^f = 14.85$ km and $L_y^f = 9.4$ km, respectively. The ratios L_{ind}/L_x^f, L_x/L_x^f and L_y/L_y^f measure 1.21, 3.37 and 3.19, respectively. We note
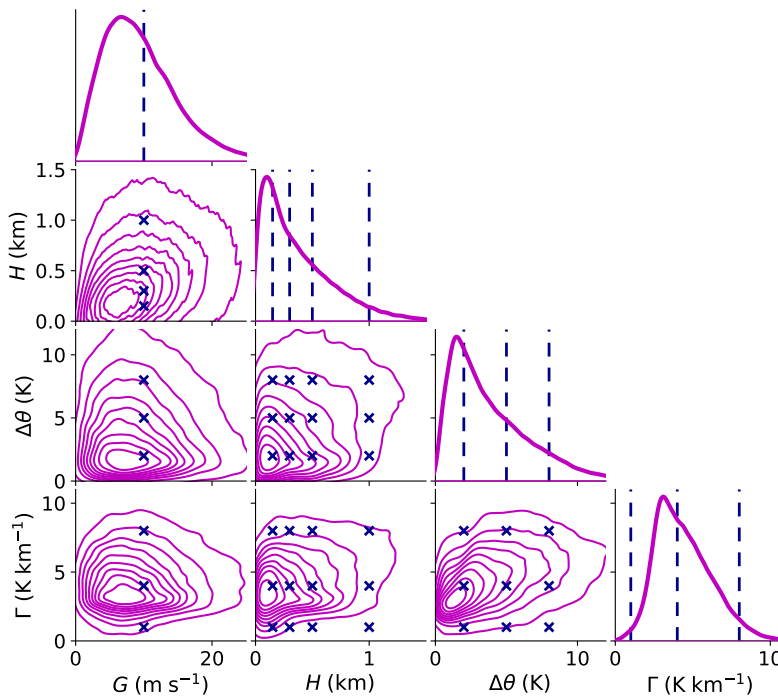
FIGURE 2. Joint probability density function of the geostrophic wind G, capping-inversion height H, capping inversion strength $\Delta\theta$ and free-atmosphere lapse rate Γ. The parameters that characterize the CNBL profile are obtained by fitting the ERA5 vertical potential temperature profile between the surface level and 2.5 km using the Rampanelli & Zardi (2004) model. The geostrophic wind is obtained by taking the mean velocity magnitude between the top of the capping inversion and 2.5 km. The blue vertical dashed lines and crosses denote the parameters selected in the current study, i.e. $G = 10$ m s^{-1}, $H = 150, 300, 500, 1000$ m, $\Delta\theta = 2, 5, 8$ K and $\Gamma = 1, 4, 8$ K km^{-1}. All combinations are considered, for a total of 36 cases.

that in the current work, we only focus on the effect of atmospheric conditions on the flow behaviour given a constant farm layout. Investigating the effects of farm density and shape is a topic for future research.

2.6. *Atmospheric state*

To select a range of relevant atmospheric states, we analyzed 30 years of ERA5 reanalysis data (from 1988 to 2018) measured at 51.6N 3.0E, which is the nearest grid point to the Belgian–Dutch offshore wind-farm cluster. We use the model proposed by Rampanelli & Zardi (2004) to fit the vertical potential temperature profile from the surface level up to 2.5 km, using a least square fit to all levels in this range. The outputs of this model consist of an estimate of the capping inversion height H and strength $\Delta\theta$ and lapse rate Γ in the free atmosphere. To evaluate the geostrophic wind, we compute the mean velocity magnitude between the top of the capping inversion and 2.5 km.

The subplots on the diagonal of Figure 2 display the probability density functions of such parameters while the joint probability density functions are shown in the off-diagonal subplots. In this study, we fix the geostrophic wind to 10 m s^{-1}, which is in line with previous studies (Abkar & Porté-Agel 2013; Wu & Porté-Agel 2017; Allaerts & Meyers 2017, 2018; Lanzilao & Meyers 2022). Moreover, this choice leads to region 2 operation of our wind farm. In regard to the capping inversion height, we select the

values of 150, 300, 500 and 1000 m, so that we can explore farm operations in shallow and deep boundary layers, including some cases where the inversion-layer base is located below the turbine-tip height. The capping inversion strength $\Delta\theta$ is set to 2, 5 or 8 K while we fix Γ to 1, 4 or 8 K km^{-1}. This wide variety of capping-inversion strengths and free lapse rates allows us to study the influence of interfacial and internal waves on farm energy extraction and flow blockage. The ground temperature and the capping-inversion thickness are fixed to $\theta_0 = 288.15$ K and $\Delta H = 100$ m for all simulations. The blue crosses in Figure 2 denote the 36 atmospheric states that we selected. Finally, we fix the latitude to $\phi = 51.6°$, which leads to a Coriolis frequency of $f_c = 1.14 \times 10^{-4}$ s^{-1}, and the surface roughness to $z_0 = 1 \times 10^{-4}$ m for all simulations. This value represents calm sea conditions and enters in the range of values observed over the North Sea, and more generally offshore (Taylor & Yelland 2000; Allaerts & Meyers 2017; Lanzilao & Meyers 2022; Kirby *et al.* 2022). More details on the atmospheric states selected and the suite of simulations performed are reported in Table 1.

In the remainder of the text, the state variables will be accompanied by a bar in case of time averages. For the horizontal averages along the full streamwise and spanwise directions, we use the angular brackets $\langle \cdot \rangle$.

3. Boundary-layer initialization

The spin-up of the precursor simulations is discussed in Section 3.1. After the spin-up phase, we start the main domain simulation and we perform a wind-farm start-up phase driven by the precursor simulation, during which the flow adjusts to the presence of the farm. This phase is discussed in Section 3.2. Finally, we discuss the methodology used to perform simulations in a neutral boundary layer (NBL) reference case in Section 3.3.

3.1. *Generation of a fully developed turbulent flow field*

The various H, $\Delta\theta$ and Γ values selected are combined together to form 36 atmospheric states, which range from a shallow boundary layer with a strong inversion layer and free atmosphere stratification, to a deep boundary layer with low $\Delta\theta$ and Γ values. The initial vertical potential-temperature profiles are generated giving the H, $\Delta\theta$ and Γ values as input to the Rampanelli & Zardi (2004) model. For the initial velocity profile, we use a constant geostrophic wind above the capping inversion. Within the ABL, we use the Zilitinkevich (1989) model with friction velocity $u_* = 0.26$ m s^{-1}. The velocity profiles below the capping inversion are then combined with the laminar profile in the free atmosphere following the method proposed by Allaerts & Meyers (2015).

Next, we add random divergence-free perturbations with an amplitude of $0.1G$ in the first 100 m to the vertical velocity profiles. This initial state is given as input to the precursor simulation. Since no turbines are located in the domain, the only drag force acting on the flow is the wall stress. The flow is advanced in time for 20 h, which is sufficient to obtain a turbulent fully developed statistically steady state (Pedersen *et al.* 2014; Allaerts & Meyers 2017; Lanzilao & Meyers 2023). Figure 3 illustrates vertical profiles of several quantities of interest averaged over the last 4 h of the simulations and over the full horizontal directions. Figure 3(a-d) shows the velocity magnitude normalized with the geostrophic wind. The boundary layer extends up to the capping inversion, which limits its growth. All velocity profiles show a common feature, that is the presence of a super-geostrophic jet near the top of the ABL. The same behaviour was previously noted also by Hess (2004) and Pedersen *et al.* (2014). We note that this phenomenon is more accentuated for the H150 cases, where a stronger wind shear along with stronger velocity gradients at the top of the ABL are attained. Next, Figure 3(e-h) displays the shear stress

Cases	H (m)	$\Delta\theta$ (K)	Γ (K km^{-1})	ΔH (m)	M_{hub} (m s^{-1})	TI_{hub} (%)	$u_\star$ (m s^{-1})	$\alpha(°)$	γ_v (−)	Fr (−)	P_N (−)	N_t (−)
H150-Δθ0-Γ0	-	0.00	0	-	9.47	3.30	0.277	-18.28	1.06	-	-	160
H150-Δθ2-Γ1	251	1.58	1	56	9.47	3.48	0.280	-15.48	1.02	2.53	5.95	160
H150-Δθ2-Γ4	245	1.95	4	48	9.48	3.48	0.280	-15.88	1.03	2.32	3.05	160
H150-Δθ2-Γ8	240	2.36	8	44	9.47	3.40	0.279	-16.29	1.07	2.08	2.11	160
H150-Δθ5-Γ1	211	4.42	1	44	9.47	3.39	0.278	-18.23	1.06	1.63	6.86	160
H150-Δθ5-Γ4	210	4.67	4	42	9.47	3.30	0.277	-18.28	1.06	1.59	3.46	160
H150-Δθ5-Γ8	209	5.00	8	42	9.47	3.32	0.277	-18.40	1.10	1.51	2.36	160
H150-Δθ8-Γ1	196	7.35	1	47	9.46	3.17	0.276	-19.30	1.09	1.30	7.22	160
H150-Δθ8-Γ4	195	7.57	4	48	9.46	3.35	0.276	-19.40	1.08	1.28	3.65	160
H150-Δθ8-Γ8	195	7.87	8	48	9.45	3.08	0.275	-19.32	1.14	1.22	2.44	160
H150-Δθ5-Γ4-st	210	4.67	4	42	9.47	3.30	0.277	-18.28	1.06	1.59	3.46	1
H300-Δθ0-Γ0	-	0.00	0	-	9.42	3.60	0.281	-12.60	0.97	-	-	160
H300-Δθ2-Γ1	348	1.95	1	57	9.38	3.66	0.280	-11.83	0.98	1.97	4.41	160
H300-Δθ2-Γ4	348	2.19	4	52	9.38	3.68	0.280	-11.87	0.98	1.85	2.20	160
H300-Δθ2-Γ8	347	2.49	8	49	9.39	3.63	0.281	-11.95	0.97	1.75	1.57	160
H300-Δθ5-Γ1	325	4.93	1	67	9.41	3.61	0.281	-12.59	0.97	1.29	4.76	160
H300-Δθ5-Γ4	325	5.15	4	66	9.42	3.60	0.281	-12.60	0.97	1.26	2.38	160
H300-Δθ5-Γ8	326	5.42	8	63	9.41	3.59	0.281	-12.55	0.98	1.22	1.66	160
H300-Δθ8-Γ1	316	7.93	1	78	9.43	3.58	0.281	-12.91	0.98	1.03	4.87	160
H300-Δθ8-Γ4	316	8.15	4	77	9.43	3.59	0.281	-12.92	0.98	1.01	2.43	160
H300-Δθ8-Γ8	316	8.46	8	76	9.43	3.58	0.282	-12.88	0.98	0.99	1.71	160
H300-Δθ5-Γ4-st	325	5.15	4	66	9.42	3.60	0.281	-12.60	0.97	1.26	2.38	1
H500-Δθ0-Γ0	-	0.00	0	-	9.24	3.93	0.277	-9.09	0.93	-	-	160
H500-Δθ2-Γ1	521	2.04	1	75	9.22	3.95	0.277	-8.94	0.91	1.60	3.04	160
H500-Δθ2-Γ4	524	2.26	4	68	9.22	3.96	0.277	-8.93	0.92	1.50	1.50	160
H500-Δθ2-Γ8	523	2.54	8	66	9.22	3.96	0.277	-8.93	0.92	1.42	1.06	160
H500-Δθ5-Γ1	507	5.05	1	90	9.24	3.92	0.278	-9.08	0.92	1.03	3.10	160
H500-Δθ5-Γ4	509	5.28	4	87	9.24	3.93	0.277	-9.09	0.93	0.99	1.54	160
H500-Δθ5-Γ8	511	5.59	8	86	9.24	3.93	0.277	-9.11	0.93	0.97	1.08	160
H500-Δθ8-Γ1	503	8.05	1	96	9.25	3.93	0.278	-9.14	0.93	0.81	3.11	160
H500-Δθ8-Γ4	504	8.29	4	94	9.25	3.93	0.278	-9.15	0.93	0.80	1.55	160
H500-Δθ8-Γ8	504	8.61	8	92	9.25	3.94	0.278	-9.15	0.91	0.79	1.11	160
H500-Δθ5-Γ4-st	509	5.28	4	87	9.24	3.93	0.277	-9.09	0.93	0.99	1.54	1
H1000-Δθ0-Γ0	-	0.00	0	-	9.13	4.18	0.275	-7.90	0.86	-	-	160
H1000-Δθ2-Γ1	1003	2.08	1	96	9.12	4.16	0.275	-7.93	0.86	1.80	1.63	160
H1000-Δθ2-Γ4	1003	2.32	4	95	9.12	4.15	0.275	-7.97	0.86	1.80	0.82	160
H1000-Δθ2-Γ8	1003	2.65	8	95	9.14	4.15	0.275	-7.88	0.86	1.80	0.58	160
H1000-Δθ5-Γ1	1001	5.08	1	99	9.13	4.16	0.275	-7.87	0.86	0.74	1.65	160
H1000-Δθ5-Γ4	1001	5.33	4	99	9.13	4.18	0.275	-7.90	0.86	0.73	0.82	160
H1000-Δθ5-Γ8	1001	5.33	8	99	9.13	4.17	0.275	-7.91	0.86	0.70	0.58	160
H1000-Δθ8-Γ1	1000	8.08	1	100	9.14	4.16	0.275	-7.92	0.86	0.59	1.64	160
H1000-Δθ8-Γ4	1001	8.33	4	100	9.13	4.16	0.275	-7.98	0.86	0.58	0.82	160
H1000-Δθ8-Γ8	1001	8.67	8	100	9.13	4.15	0.275	-7.99	0.86	0.57	0.58	160
H1000-Δθ5-Γ4-st	1001	5.33	4	99	9.13	4.18	0.275	-7.90	0.86	0.73	0.82	1

TABLE 1. Overview of the spin-up cases used to drive 40 wind-farm simulations and 4 single-turbine simulations. The parameters are averaged over the last 4 h of the spin-up phase and include the capping-inversion height H, the capping-inversion strength $\Delta\theta$, the free atmosphere lapse rate Γ, the capping-inversion thickness ΔH, the turbulence intensity measured at hub height TI_{hub}, the velocity magnitude measure at hub height M_{hub}, the friction velocity $u_\star$, the geostrophic wind angle α, the shape factor γ_v, the Froude number Fr, the P_N number and the number of turbines N_t. Note that the parameters H, $\Delta\theta$, Γ and ΔH have been estimated by fitting the spin-up profiles averaged over the last 4 h of the precursor simulations with the Rampanelli & Zardi (2004) model.

magnitude, which is non-zero only below the capping inversion, with a quasi-linear profile. We note that varying $\Delta\theta$ and Γ results in very minor differences in terms of velocity and shear stresses. Next, Figure 3(i-l) shows the flow angle. At turbine-hub height, the flow is parallel to the x-direction. This is achieved by using the wind-angle controller developed and tuned by Allaerts & Meyers (2015), which is designed to ensure a desired orientation of the hub-height wind direction ($\Phi_d = 0°$ in this case). Below the turbine-tip height, the flow is almost unidirectional since most of the wind-direction change occurs within the inversion layer, expects for deep boundary layers. The geostrophic wind angle, which is the angle between the surface stress and the geostrophic wind velocity, is larger for shallow boundary layers, as noted by Allaerts & Meyers (2017). Finally, the thermal stratification is illustrated in Figure 3(m-p) by means of potential temperature profiles.

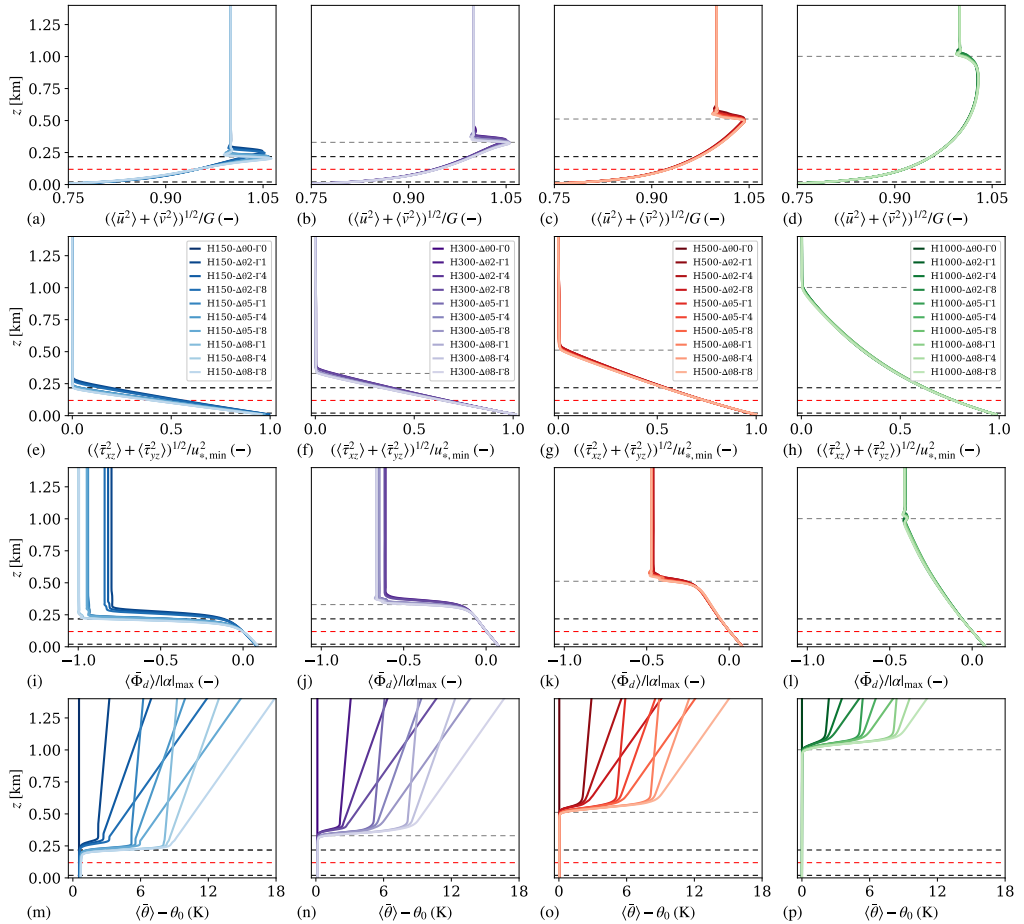The various spin-up cases together with some parameters of interest averaged over

FIGURE 3. Vertical profiles of (a-d) velocity magnitude, (e-h) shear stress magnitude, (i-l) wind direction and (m-p) potential temperature averaged along the full horizontal directions and over the last 4 h of simulation. The results are shown for (a,e,i,m) H150, (b,f,j,n) H300, (c,g,k,o) H500 and (d,h,l,p) H1000 cases using various capping-inversion strengths and free-atmosphere lapse rates. Moreover, the profiles are further normalized with $G = 10$ m s^{-1}, $u_{\star,min} = 0.275$ m s^{-1}, $|\alpha|_{max} = 19.4°$ and $\theta_0 = 288.15$ K. The red dashed line denotes the turbine-hub height while the black dashed lines are representative of the rotor dimension. Finally, the grey dashed line represents the averaged inversion-layer height.

the last 4 h of simulation are summarized in Table 1. During the spin-up phase, the capping-inversion height moves slightly upward. The increase in inversion-layer height is more accentuated for the shallow boundary-layer cases. For instance, the H150 cases show a growth of 67 m on average over the 20 h of spin-up. For the H1000 cases, the boundary-layer height remains unaltered. This result is consistent with the equilibrium theory of Csanady (1974) and with previous LES findings (Pedersen *et al.* 2014; Allaerts & Meyers 2015, 2017). The capping-inversion strength slightly increases for the majority of the cases while the free-atmosphere stratification remains unchanged. The velocity magnitude at turbine-hub height varies between 9.1 and 9.5 m s^{-1} among all cases, meaning that turbines operate in the region 2 (Bortolotti *et al.* 2019). Moreover, the turbulence intensity at turbine-hub height varies from 3.3% to 4.1%. These values are in line with the ones observed by Barthelmie *et al.* (2009) and Türk & Emeis (2010)
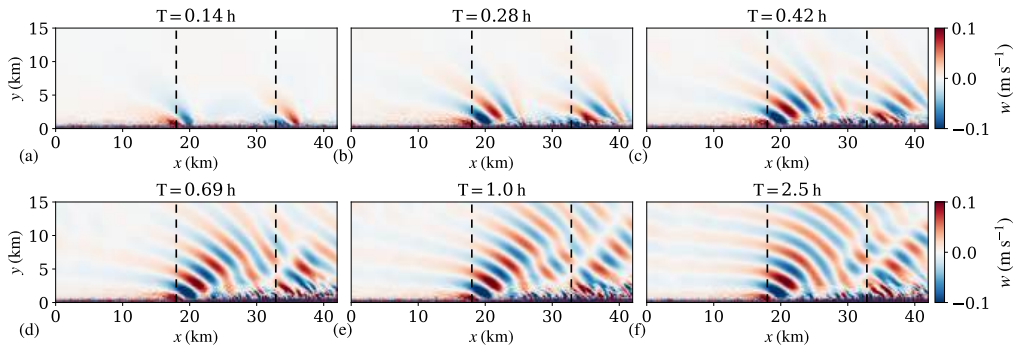
FIGURE 4. Instantaneous contours of vertical velocity for case H500-$\Delta\theta$2-Γ8 obtained (a-d) during the wind-farm start-up phase, (e) at the end of the wind-farm start-up phase and (f) at the end of the simulation. The x–z plane is taken along the centerline of the domain, i.e. at $y = 15$ km. The black vertical dashed lines denote the location of the first- and last-row turbine. We note that the fringe region and RDL are not displayed in the plots.

over the North Sea. The large variance in the Froude number, defined as $Fr = U_B/\sqrt{g'H}$ with U_B the bulk velocity along the x-direction and $g' = g\Delta\theta/\theta_0$ the reduced gravity, will allow us to analyze the flow response to wind-farm forcing under critical ($Fr \approx 1$), sub-critical ($Fr \lessgtr 1$) and super-critical ($Fr \gtrless 1$) conditions with varying $P_N = U_B^2/NGH$ numbers. Both the Fr and P_N number values are reported in Table 1.

3.2. *Wind-farm start-up phase*

The turbulent fully-developed inflow profiles previously discussed are now used to drive the simulation in the main domain, where the turbines impose a drag force on the flow. However, before collecting flow statistics over time, a second spin-up phase is required. In fact, the flow has to adjust to the presence of the farm in the main domain before reaching a new statistically-steady state. We name this phase wind-farm start-up. Figure 4 shows the time evolution of the vertical velocity field on an x–z plane for case H500-$\Delta\theta$2-Γ8. The flow divergence induced by the farm drag force displaces upward the capping inversion, which in turn triggers a first train of internal gravity waves in proximity to the first-row turbine location. Vice versa, the flow convergence in the farm wake moves the capping inversion downward, generating a second train of internal waves at the last-row turbine location. This is clearly visible in Figure 4(a). The two out-of-phase trains of waves are convected downstream, until they eventually merge at T=1 h, as shown in Figure 4(e). At this point, the numerical solution is further advanced in time for 1.5 h. The instantaneous vertical velocity flow field taken at T=2.5 h is displayed in Figure 4(f). By comparing the numerical solution at T=1 h against the one obtained at T=2.5 h, we notice minimal differences. A similar behaviour is observed for the streamwise and spanwise velocity field (not shown). This means that 1 h of wind-farm spin-up time suffices for the flow to adjust to the farm drag force. Therefore, similarly to Allaerts & Meyers (2017) and Lanzilao & Meyers (2022), we fix the duration of the wind-farm start-up phase to 1 h, which corresponds to roughly two and a half wind-farm flow-through times. Next, we switch off the wind-angle controller in the precursor simulation and we collect statistics during a time window of 1.5 hour.

3.3. *Construction of a neutral boundary layer reference case*

For each inversion-layer height, we also include a case characterized by the absence of the capping inversion and a neutral free atmosphere, an idea originally proposed by
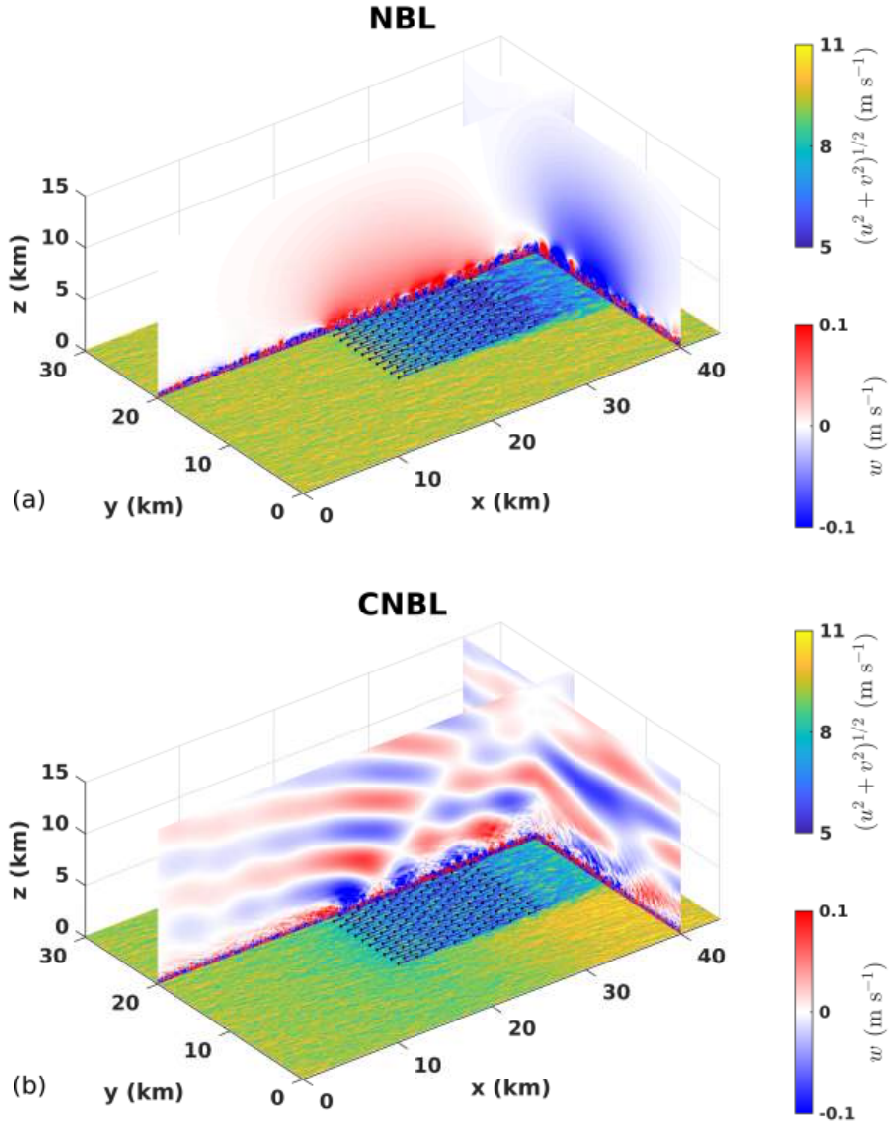
FIGURE 5. Snapshot of the instantaneous flow field obtained after 2.5 hour of simulation time in the (a) NBL reference case and in (b) CNBL conditions. The two simulations correspond to cases H500-$\Delta\theta$0-Γ0 and H500-$\Delta\theta$5-Γ4, respectively. The x–y plane shows contours of velocity magnitude $(u^2 + v^2)^{1/2}$ taken at turbine-hub height while the x–z and y–z planes display the vertical velocity field. The black disks denote the wind-turbine rotor locations. Finally, we note that the fringe region and RDL are not displayed. We remark that the only difference in the NBL reference case consists in the absence of thermal stratification above the ABL and therefore gravity waves.

Lanzilao & Meyers (2022). To do so, the fringe forcing in the main domain only forces the velocity field to the one provided by the CNBL developed in the precursor domain, leaving the potential temperature constant with height. To give an example, case H500-$\Delta\theta$0-Γ0 is driven by the flow fields obtained in the precursor simulation of case H500-$\Delta\theta$5-Γ4, but sets the temperature profile in the main domain to a constant value. Consequently, in this

case, the farm operates under the same turbulent inflow velocity profile but in the absence of atmospheric gravity waves. This is admittedly a numerical construction that does not really exist in reality but allows us to factor out the free-atmosphere stratification effects. It has however also some drawbacks. For instance, the capping-inversion height is much lower than the Ekman-layer equilibrium height that the boundary layer would attain in a TNBL. Therefore, in the main domain, the flow within the ABL inevitably starts mixing with the free atmosphere, varying its shear and veer already before reaching the first-row turbine location. In the H150-Δθ0-Γ0 and H300-Δθ0-Γ0 cases, this flow mixing is very high, varying considerably the flow profiles. For instance, the flow angle at the farm entrance measures approximately 10° in the H150-Δθ0-Γ0 case. However, this effect becomes negligible in the H500-Δθ0-Γ0 and H1000-Δθ0-Γ0 cases, where the flow remains parallel to the streamwise direction and in general profiles show very similar results in front of and across the farm, with a farm efficiency of 47.0% and 46.7%, respectively. Therefore, we use case H500-Δθ0-Γ0 as a reference simulation for a farm operating in the absence of thermal stratification above the ABL in the rest of this manuscript, and we refer to it as the NBL reference case.

A working example of this idea is given in Figure 5(a,b), which displays the flow field obtained in the main domain for the NBL reference case (i.e. H500-Δθ0-Γ0) and the H500-Δθ5-Γ4 case, respectively. The two simulations are driven by the same turbulent inflow profiles. However, the potential-temperature profile is set to a constant in Figure 5(a) while Figure 5(b) uses the potential temperature provided by the precursor simulations. By comparing the results of these two simulations, it is easy to investigate the effects induced by the thermal stratification above the ABL on the wind-farm flow behaviour. The various differences will be analyzed in detail in Section 5.

4. Sensitivity of wind-farm performance to the domain length and width

The numerical domain should be wide enough to limit artificial sidewise blockage. The latter occurs when the lateral boundaries are too close to the farm. Moreover, enough streamwise distance should be present upwind of the farm, to properly account for the flow deceleration due to the wind-farm blockage effect. Similarly, the fringe region should be located far enough from the last-turbine row to avoid spurious effects on the flow development in proximity to the farm. In the presence of neutral atmospheres, these numerical artefacts have a very limited impact on the farm performance. In fact, the absence of free-atmosphere stratification reduces the wind-farm footprint, allowing for a smaller numerical domain. This is clearly visible in Figure 5(a). However, the effects of the domain boundaries can significantly alter the wind-farm performance when thermal stratification above the ABL is considered. To date, there are no guidelines on how to select the domain length and width when performing simulation in CNBLs. The goal of this section is to define such criteria.

To this end, we first fix a relatively small reference domain with L_x and L_y equal to 40 and 20 km, respectively, which correspond to a typical domain length and width used in previous studies (Allaerts & Meyers 2017, 2018; Lanzilao & Meyers 2022, 2023). Thereafter, we first keep L_y constant and we vary L_x between 40 and 80 km, so that the fetch of the domain from the inflow to the first-row turbine location (i.e. L_{ind}) varies between 10 and 50 km, respectively. This corresponds to a ratio L_{ind}/L_x^f of 0.67 and 3.37. Next, we keep L_x constant and we vary L_y between 20 and 60 km, so that the ratio L_y/L_y^f goes from 2.13 to 6.38, respectively. In total, we end up with seven domain configurations, which are illustrated in Figure 6. We note that all simulations adopt a
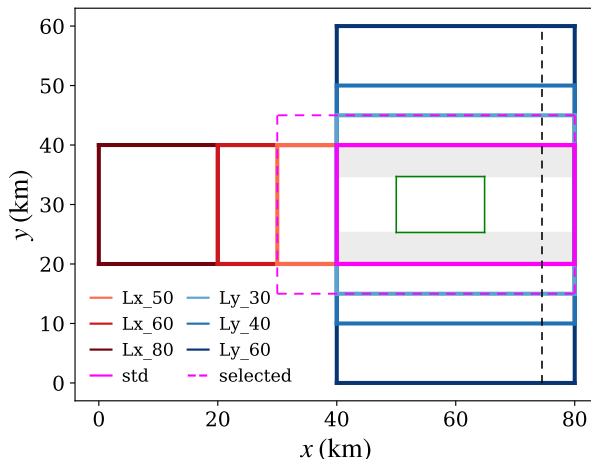
FIGURE 6. Sketch of the numerical-domain length and width adopted in the sensitivity study. The dashed pink rectangle denotes the domain selected for performing the sensitivity study to the atmospheric state. Moreover, the green rectangle represents the wind-farm dimension while the vertical dashed black line denotes the starting point of the fringe region. Finally, the grey shaded areas and the region in between them represent the areas over which spanwise averages are taken by the operator $\langle\cdot\rangle_s$ and $\langle\cdot\rangle_f$, respectively.

Cases	L_x (km)	L_y (km)	L_z (km)	L_{ind}/L_x^f (–)	L_y/L_y^f (–)	N_x (–)	N_y (–)	N_z (–)	DOF (–)
std	40	20	25	0.67	2.13	1280	920	490	2.89×10^9
Lx-50	50	20	25	1.35	2.13	1600	920	490	3.46×10^9
Lx-60	60	20	25	2.02	2.13	1920	920	490	4.04×10^9
Lx-80	80	20	25	3.37	2.13	2560	920	490	5.19×10^9
Ly-30	40	30	25	0.67	3.19	1280	1380	490	4.33×10^9
Ly-40	40	40	25	0.67	4.26	1280	1840	490	5.77×10^9
Ly-60	40	60	25	0.67	6.38	1280	2760	490	8.66×10^9
selected	50	30	25	1.21	3.19	1600	1380	490	5.19×10^9

TABLE 2. Overview of the numerical domains used to perform the sensitivity study on the domain size. The parameters L_x, L_y and L_z denote the streamwise, spanwise and vertical domain dimensions while N_x, N_y and N_z denote the number of grid points used along the respective directions. Moreover, L_{ind} denotes the fetch of domain between the inflow and the first-row turbine location while L_x^f and L_y^f represent the wind-farm length and width, respectively. The last column reports the number of DOF comprehensive of both precursor and main domains. We note that each case is driven by three different CNBLs, that is H300-$\Delta\theta$5-Γ4, H500-$\Delta\theta$5-Γ4 and H1000-$\Delta\theta$5-Γ4, for a total of 21 simulations. Finally, the last row reports the selected domain used to perform the sensitivity study to the atmospheric state.

vertical domain height of 25 km and have the same grid resolution. Since we speculate that the domain size should scale with the height of the capping inversion, we drive these simulations with three different inflow profiles with equal $\Delta\theta$ and Γ but different H, that is H300-$\Delta\theta$5-Γ4, H500-$\Delta\theta$5-Γ4 and H1000-$\Delta\theta$5-Γ4, for a total of 21 simulations. The various cases analyzed in this section are summarized in Table 4. Finally, we note that the notations $\langle\cdot\rangle_f$ and $\langle\cdot\rangle_s$ are used to represent spanwise averages along the width of the farm (i.e. from first to last turbine column) and at its side, respectively. In case of a horizontal average over the full spanwise direction and along the turbine-rotor height or capping-
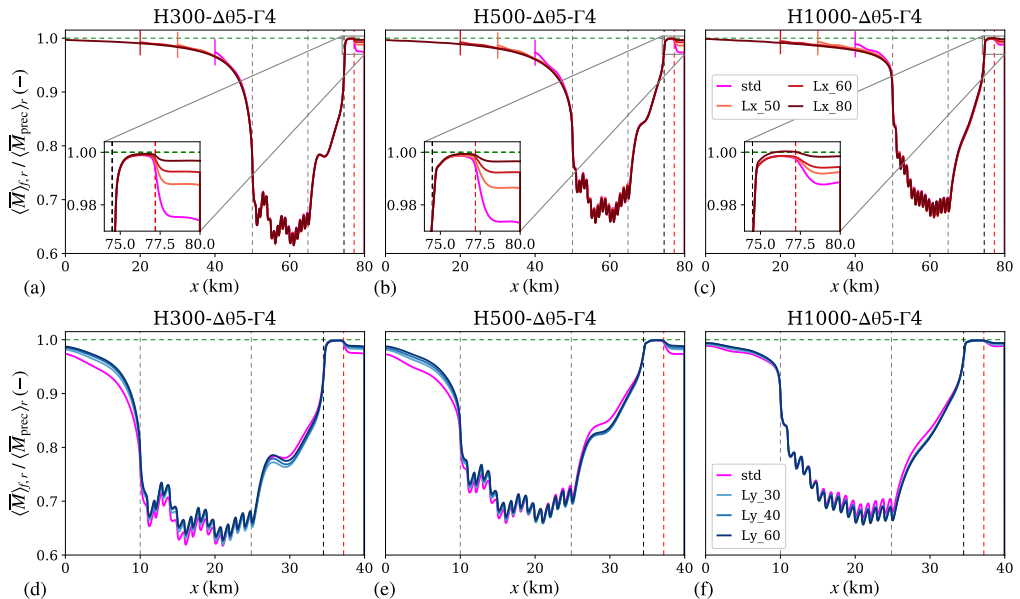
FIGURE 7. Time-averaged velocity magnitude $M = (u^2 + v^2)^{1/2}$ averaged in the horizontal direction along the farm width and in height along the turbine rotor. We normalize the results with the velocity magnitude obtained in the precursor simulation and we plot it as a function of the streamwise direction. Results are shown for different (a-c) domain lengths and (d-f) domain widths. The simulations are driven by the cases (a,d) H300-$\Delta\theta$5-Γ4, (b,e) H500-$\Delta\theta$5-Γ4 and (c,f) H1000-$\Delta\theta$5-Γ4. The grey vertical dashed lines are positioned in correspondence of the first- and last-row turbines. Moreover, the black and red vertical dashed lines denote the starting and ending point of the fringe forcing. The fringe region extends to the domain end to account for the damping of the convective term. In the bottom left corner of panels (a-c), the flow behaviour within the fringe region is magnified. Finally, the vertical segments in panels (a-c) facilitate the identification of the starting points of the domains with smaller L_x.

inversion thickness, we adopt the notation $\langle \cdot \rangle_r$ and $\langle \cdot \rangle_c$, respectively. For instance, the notation $\langle \cdot \rangle_{f,r}$ represents a spanwise average over the farm width and a vertical average over the turbine-rotor height. We refer to Figure 6 for more details.

Figure 7(a) shows the time-averaged velocity magnitude further averaged in the horizontal directions along the farm width and in height along the turbine rotor. We scale the plot with the velocity magnitude obtained in the precursor simulation. Here, the results refer to domains of different lengths driven by the H300-$\Delta\theta$5-Γ4 case. Interestingly, the large L_{ind} value in the Lx_80 case allows us to observe that the flow begins to slow down several tens of kilometers upstream of the farm. Within the farm, the effect of turbines and wake mixing is clearly visible. In the last 5.5 kilometers of the domain, the body force applied within the fringe region restores the inflow provided by the precursor simulation. Surprisingly, the solutions obtained on shorter domains follow the same trend and also have the same magnitude. In fact, the convective damping region within the fringe region seems to indirectly account for the additional flow slow down necessary to match the solution obtained on longer domains. Figure 7(b,c) shows that the same behaviour is attained for deeper boundary layers.

The numerical solution is much more sensitive to the domain width. This is illustrated in Figure 7(d), which shows the velocity magnitude obtained with domains of different widths driven by the H300-$\Delta\theta$5-Γ4 case. Here, the solution obtained on the standard domain has a velocity that is 1.5% lower than case Ly_60 at $x = 0$ km. This additional
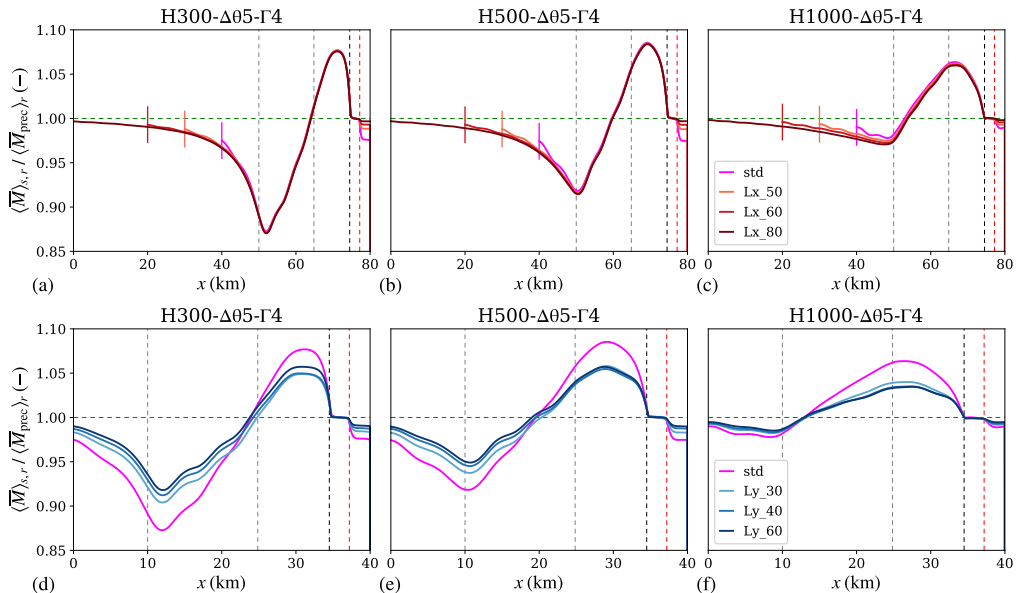
FIGURE 8. Time-averaged velocity magnitude $M = (u^2 + v^2)^{1/2}$ averaged in the horizontal directions along the farm sides and in height along the turbine rotor. We normalize the results with the velocity magnitude obtained in the precursor simulation and we plot it as a function of the streamwise direction. Results are shown for different (a-c) domain lengths and (d-f) domain widths. The simulations are driven by the cases (a,d) H300-$\Delta\theta5$-$\Gamma4$, (b,e) H500-$\Delta\theta5$-$\Gamma4$ and (c,f) H1000-$\Delta\theta5$-$\Gamma4$. The grey vertical dashed lines are positioned in correspondence of the first- and last-row turbines. Moreover, the black and red vertical dashed lines denote the starting and ending point of the fringe forcing. The fringe region extends to the domain end to account for the damping of the convective term. Finally, the vertical segments in panels (a-c) facilitate the identification of the starting points of the domains with smaller L_x.

slow down is purely artificial and comes from the fact that L_y/L_y^f measures only 2.12 in the standard domain. The same difference reduces to 0.5% for the deep boundary layer case – see Figure 7(f). This is expected since the influence of the inversion layer on the flow behaviour is inversely related to its height.

The results in terms of velocity magnitude averaged in the horizontal directions along the farm sides (i.e. the shaded areas in Figure 6) and in height along the turbine rotor are shown in Figure 8. Again, when varying L_x all solutions collapse onto the one obtained with the standard domain. However, considerable differences are observed in Figure 7(d-e), where we vary the domain width. In fact, the presence of the inversion layer limits the boundary-layer thickening, causing the flow to accelerate at the farm sides. A narrow domain artificially enhances this channelling effect of about 2% in terms of velocity magnitude. As the inversion-layer height increases, solutions on wider domains tend to collapse onto each other.

Finally, for a quantitative estimate of the influence of the domain length and width on wind-farm performance, we look at the farm efficiencies. Hence, similarly to Allaerts & Meyers (2018), we define the farm efficiency as $\eta_f = \eta_w \eta_{nl}$, with

$$\eta_w = \frac{P_{\text{tot}}}{N_t P_1}, \qquad \eta_{nl} = \frac{P_1}{P_\infty} \tag{4.1}$$

where η_w and η_{nl} denote the wake and non-local efficiency, respectively. Moreover, N_t indicates the number of turbines, P_{tot} the total farm power, P_1 the averaged power
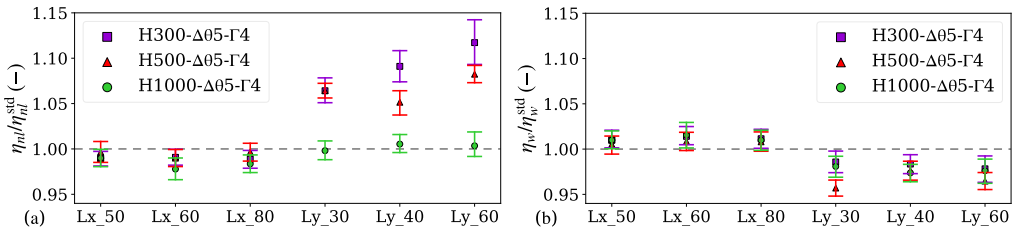
FIGURE 9. (a) Non-local and (b) wake efficiency normalized by the values obtained in the standard domain. The symbol denotes the time-averaged value while the error bars represent the 95% confidence interval. The latter are computed using the moving block bootstrapping method developed by Beyaztas *et al.* (2017) and Boufidi *et al.* (2020), using the procedure described by Bon & Meyers (2022).

output of first-row turbines while P_∞ represents the power output of a turbine operating in isolation. The latter is evaluated using the single-turbine simulations discussed in Appendix A.

Figure 9(a) shows that the time-averaged non-local efficiency normalized with the value obtained in the standard domain is quasi-independent on the distance between the first-row turbine and the main domain inflow, i.e. on the ratio $L_{\rm ind}/L_x^f$. This is expected in light of the results shown in Figure 7(a-c). However, considerable differences are observed when varying the domain width in shallow boundary layers. For instance, the time-averaged non-local efficiency obtained in case Ly_60 driven by H300-$\Delta\theta$5-Γ4 is 1.12 times higher than the one measured in the standard domain. The wake efficiency, shown in Figure 9(b), is less dependent on the numerical domain size and it shows a negative correlation with respect to η_{nl}.

In conclusion, the wind-farm performance is quasi-independent of the distance between the domain inflow and the first-row turbine location when using the wave-free fringe region technique. However, a narrow domain artificially enhances flow blockage. Finally, we observe that the domain size should depend upon the inversion-layer height. In fact, shallower boundary layers require wider domains than deeper ones. This also implies that wind-farm–LESs in CNBLs should adopt wider domains than simulations in neutral atmospheres. As a result of this study, we fix the main domain length and width to 50 and 30 km, respectively, with $L_{\rm ind}$ = 18 km. A sketch of this domain is reported in Figure 6. We remark that this choice is mainly dictated by the computational resources at our disposal. In fact, an even wider domain would have been relevant. Based on the current analysis, we conclude that we may overestimate the effect of blockage on farm efficiency with a factor of roughly 1.05 for $H \leqslant 500$ m, while the effect of blockage is properly represented for the H1000 cases. We note that the RDL and fringe region will be left out of the figures in the remainder of the text.

5. Sensitivity of wind-farm performance to the atmospheric state

The wind-farm flow development under various atmospheric conditions is examined in this section. First, we perform a qualitative analysis on the separate effects of varying the capping-inversion height, strength and free-atmosphere lapse rate on farm performance in Sections 5.1 and 5.2, respectively. Next, we compare the LES results against various one- and two-dimensional gravity-wave linear-theory models in Section 5.3. Thereafter, we carry out a quantitative comparison in terms of state variables among all simulation cases in Section 5.4. Finally, the column-averaged wind-farm power output is presented in Section 5.5, followed by a discussion on the non-local, wake and farm efficiencies in
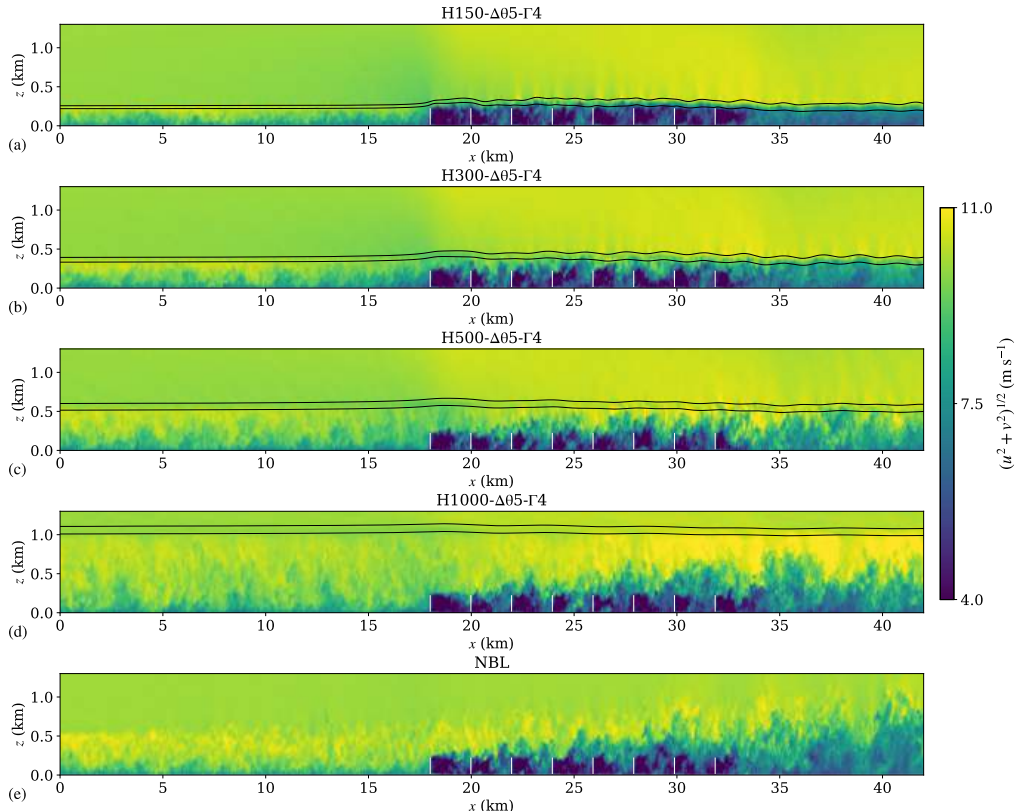
FIGURE 10. Contours of the instantaneous horizontal velocity magnitude in an x–z plane taken across the 6th column of turbines, i.e. at $y = 15.25$ km, for cases (a) H150-$\Delta\theta5$-$\Gamma4$, (b) H300-$\Delta\theta5$-$\Gamma4$, (c) H500-$\Delta\theta5$-$\Gamma4$, (d) H1000-$\Delta\theta5$-$\Gamma4$ and (e) the NBL reference case. The black lines represent the bottom and top of the inversion layer computed with the Rampanelli & Zardi (2004) model. Finally, the location of the turbine-rotor disks is indicated with vertical white lines. The NBL reference case refers to simulation H500-$\Delta\theta0$-$\Gamma0$.

Section 5.6, where we also propose a new scaling parameter for the ratio of the non-local to wake efficiency.

5.1. *Effects of the inversion-layer height on the flow development*

We start our analysis with Figure 10, which shows the x–z plane across the 6th column of turbines of the instantaneous horizontal velocity magnitude together with the base and top of the inversion layer computed by fitting the LES data with the Rampanelli & Zardi (2004) model. Every turbine imparts a force on the flow, generating a patch of low wind speed downwind. Figure 10(a) shows that such velocity deficits are very strong in a shallow boundary layer. In fact, the turbine-tip height is in close proximity to the capping-inversion base, which limits energy entrainment and therefore flow mixing, slowing down the wake recovery process. Moreover, this also limits the growth of the internal boundary layer (IBL) generated by the wind-turbine wakes expansion. Therefore, to conserve mass, the flow deceleration is mostly compensated by a flow redirection at the sides of the farm, generating high-speed flow channels. This is visible in Figure 11(a), which shows the time-averaged turbine-orientation angle with respect to the streamwise direction for all turbines in the farm. Here, the angles between the first- and last-turbine columns vary
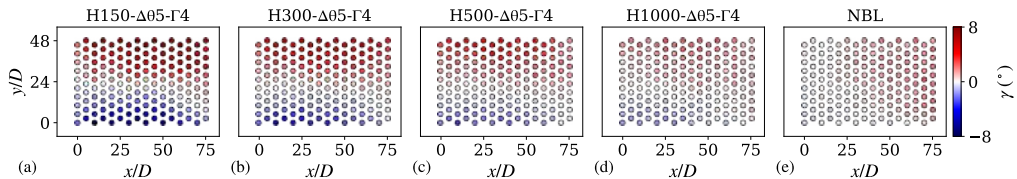
FIGURE 11. Turbine-orientation angle with respect to the streamwise direction for cases (a) H150-$\Delta\theta5$-$\Gamma4$, (b) H300-$\Delta\theta5$-$\Gamma4$, (c) H500-$\Delta\theta5$-$\Gamma4$, (d) H1000-$\Delta\theta5$-$\Gamma4$ and (e) the NBL reference case. The latter refers to simulation H500-$\Delta\theta0$-$\Gamma0$.

between $-8°$ and $8°$. The asymmetry with respect to the domain centerline observed in Figure 11 is due to the presence of the Coriolis effects. The upward motion caused by the strong flow divergence results in a capping-inversion vertical displacement, which reaches a maximum in proximity to the second-row turbines, with a relative capping-inversion displacement of 42.9%. A strong wind-speed reduction is also observed in the farm induction region. Further, the low level of energy entrainment also causes a strong wind-farm wake. The interaction between the IBL and capping inversion decreases as H increases. We observe in Figure 10(c) that the vertical wake expansion reaches the inversion-layer height only in the farm wake.

For a deep boundary layer, the capping-inversion effects on the wind-farm response become negligible. Here, the IBL does not interact with the inversion layer. This also allows a high-speed flow region to form between the IBL and capping inversion base, as shown in Figure 10(d), which enhances flow mixing and consequently the vertical transport of energy, therefore replenishing the turbine and farm wake at a higher rate. This also translates into a much smaller flow redirection at the farm sides since the vertical expansion of the IBL is not constrained by the inversion layer. Figure 11(d) shows variation in turbine-orientation angles only between $-2°$ and $2°$ for this case. In all atmospheres with thermal stratification above the ABL, Figure 10 shows that the turbulent structures are damped by the inversion layer, leaving the free atmosphere non-turbulent. A different behaviour is observed in Figure 10(e), which illustrates the results obtained in a neutral atmosphere. The turbulence structures at the top of the boundary layer are not damped by buoyant forces in this case, allowing the IBL to reach higher altitudes. Here, the reduction in wind speed caused by the turbines is solely balanced by the boundary-layer thickening. In fact, Figure 11(e) shows that all turbines have positive orientation angles, which gradually increase towards the last row.

The upward displacement of the inversion layer, which has to be considered as an interfacial wave, brings air with a lower potential temperature to a higher altitude, generating a cold anomaly. This is illustrated in Figure 12, which shows the x–z plane of the time-averaged potential-temperature perturbation field together with the base and top of the inversion layer, averaged in the horizontal directions along the farm width. The negative perturbation in the potential-temperature field is about 7 K and 2 K in cases H150-$\Delta\theta5$-$\Gamma4$ and H1000-$\Delta\theta5$-$\Gamma4$, respectively. This considerable difference is caused by the higher inversion-layer displacement attained in case H150-$\Delta\theta5$-$\Gamma4$ (and in shallow boundary-layer flows, in general), which measures 42.9% (i.e. 90 m) against the 3.8% (i.e. 40 m) obtained for case H1000-$\Delta\theta5$-$\Gamma4$. We note that the cold anomaly extends to the farm induction region in all cases. Moreover, the interfacial waves along the capping inversion are also clearly visible. In fact, Figure 12 shows that the interfacial-wave crests correspond to high potential-temperature perturbations. Finally, the flow acceleration in the wind-farm wake pushes the inversion layer downward, generating a hot anomaly.
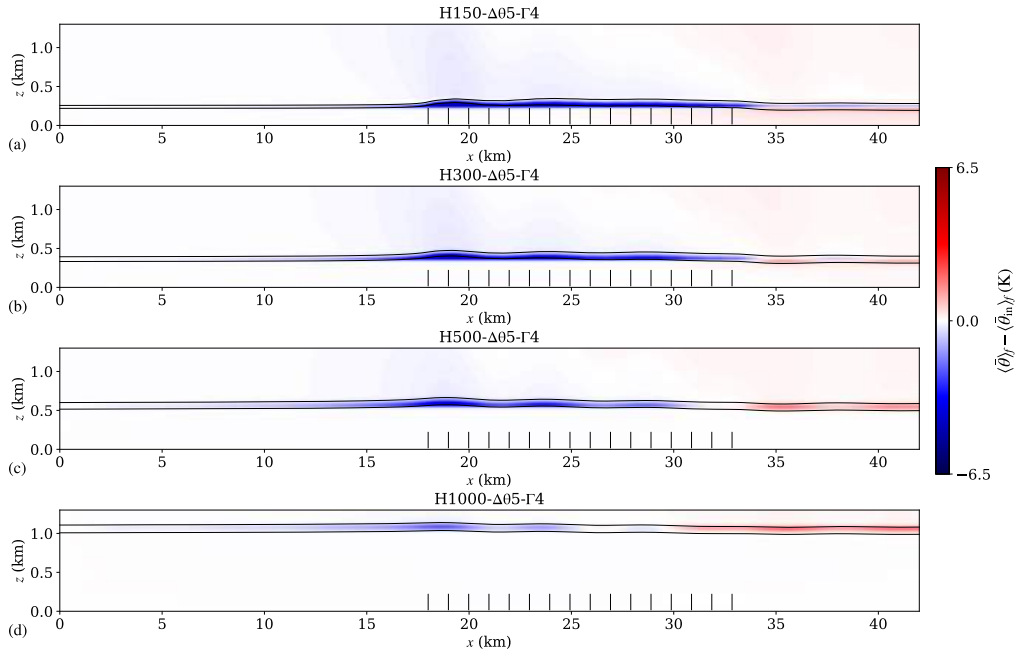
FIGURE 12. Contours of the time-averaged potential-temperature perturbation with respect to the inflow in an x–z plane further averaged in the y-direction along the width of the farm for cases (a) H150-$\Delta\theta5$-$\Gamma4$, (b) H300-$\Delta\theta5$-$\Gamma4$, (c) H500-$\Delta\theta5$-$\Gamma4$ and (d) H1000-$\Delta\theta5$-$\Gamma4$. The black lines represent the bottom and top of the inversion layer computed with the Rampanelli & Zardi (2004) model. Finally, the location of the turbine-rotor disks is indicated with vertical black lines.

Since the ABL itself is neutral, potential-temperature perturbations do not occur below the inversion layer.

As noted by Smith (2010) and Allaerts & Meyers (2017), variations in the potential-temperature field are strongly correlated to pressure perturbations. In fact, a cold anomaly translates into a higher column of cold and heavy air, which locally increases pressure. Vice versa, a hot anomaly generates a region of low pressure. This behaviour is illustrated in Figure 13, which shows an x–z plane of the time-averaged pressure-perturbation field together with the base and top of the inversion layer, averaged in the horizontal directions along the farm width. The strong cold anomaly generated in shallow boundary layers gives rise to strong increases in pressure, with a peak in the farm entrance region. This strong counteracting pressure gradient extends across the whole farm induction region. By comparing Figure 13(a,d), it becomes clear that the unfavourable pressure gradient is inversely proportional to the capping-inversion height. The low pressure region downwind of the farm generated by the hot anomaly gives rise to a favourable pressure gradient across the farm, which acts as an energy source and enhances the wake recovery mechanism. Finally, Figure 13(e) shows the pressure perturbation in an atmosphere that does not support gravity waves. Here, the unfavourable pressure gradient, which is solely due to the flow slow down caused by the cumulative turbine induction, is an order of magnitude lower than the one obtained in stratified atmospheres and only extends up to roughly six rotor diameters upstream of the first-row turbines. Moreover, also the favourable pressure gradient is negligible when compared to the one obtained in the presence of atmospheric gravity waves.
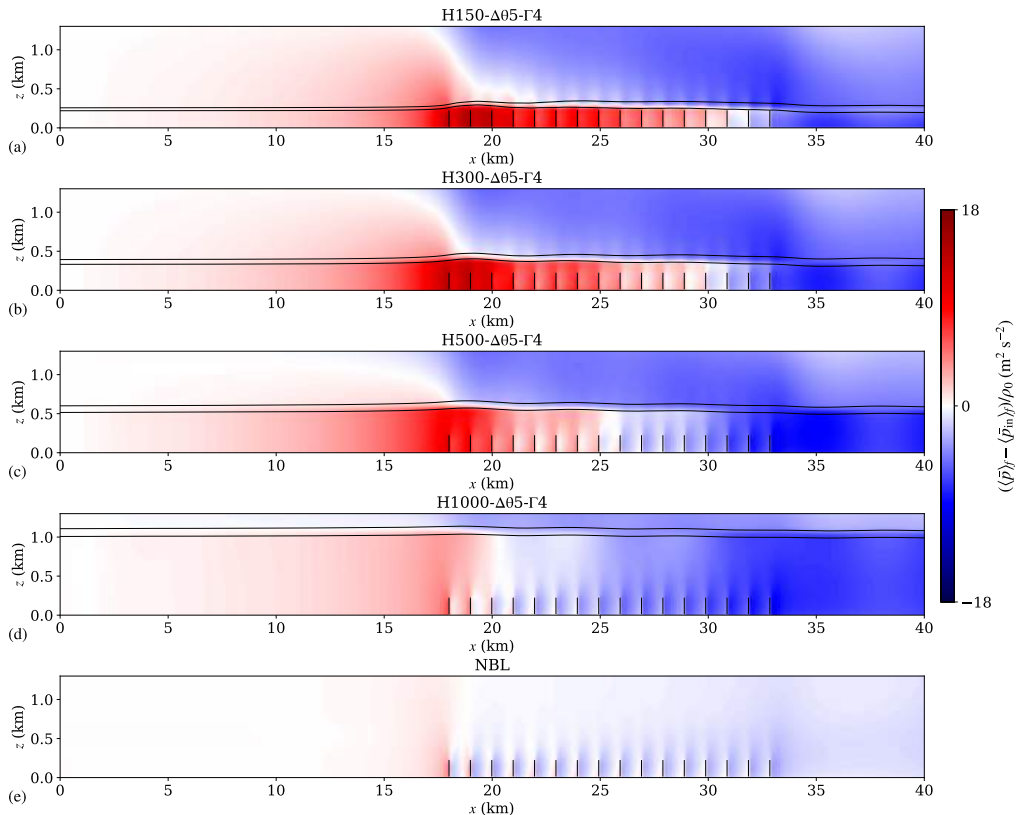
FIGURE 13. Contours of the time-averaged pressure perturbation with respect to the inflow in an x–z plane further averaged in the y-direction along the width of the farm for cases (a) H150-$\Delta\theta$5-Γ4, (b) H300-$\Delta\theta$5-Γ4, (c) H500-$\Delta\theta$5-Γ4, (d) H1000-$\Delta\theta$5-Γ4 and (e) the NBL reference case. The black lines represent the bottom and top of the inversion layer computed with the Rampanelli & Zardi (2004) model. Finally, the location of the turbine-rotor disks is indicated with vertical black lines. The NBL reference case refers to simulation H500-$\Delta\theta$0-Γ0.

5.2. *Effects of the inversion-layer strength and free-atmosphere lapse rate on the flow development*

Following the work of Klemp & Lilly (1975) and Vosper (2004), Sachsperger *et al.* (2015) derived a two-dimensional gravity-wave linear model in which they found out that the wavenumber k_x of the interfacial waves depends upon the capping-inversion strength and Brunt–Väisälä frequency as follows:

$$k_x = \frac{g\Delta\theta}{2U_B^2\theta_0} + \frac{N^2\theta_0}{2g\Delta\theta}. \tag{5.1}$$

Since the interfacial-wave horizontal wavelength is defined as $\lambda_x = 2\pi/k_x$, they showed that λ_x and $\Delta\theta$ are inversely related. Consequently, a stronger capping inversion supports interfacial waves with a lower wavelength. This is visible in Figure 14, where we compare x–y planes taken at turbine-hub height of velocity magnitude, vertical velocity and pressure perturbation of three simulations where the only varying parameter is $\Delta\theta$. Figure 14(a-c) shows that a higher $\Delta\theta$ causes a higher flow speed up at the farm sides. This is due to the fact that, on average, a high inversion-layer strength reduces the capping-inversion upward displacement. Consequently, the flow rate at the farm sides has to increase to
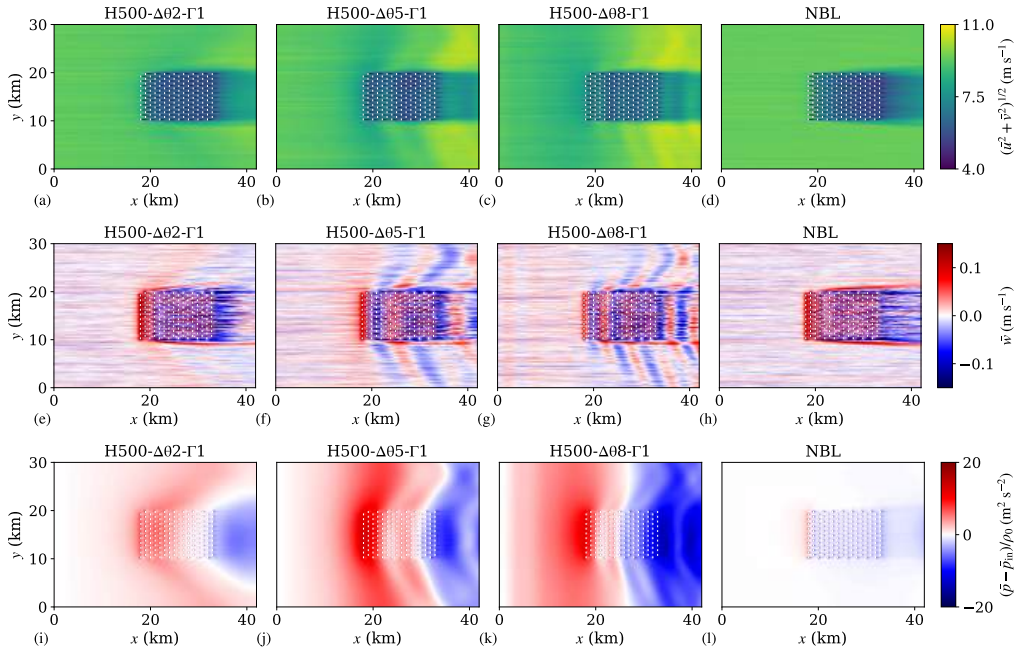
FIGURE 14. Contours of the time-averaged (a-d) velocity magnitude, (e-h) vertical velocity and (i-l) pressure perturbation in an x–y plane taken at turbine-hub height for cases (a,e,i) H500-$\Delta\theta$2-Γ1, (b,f,j) H500-$\Delta\theta$5-Γ1, (c,g,k) H500-$\Delta\theta$8-Γ1 and (d,h,l) the NBL reference case. The location of the turbine-rotor disks is indicated with vertical white lines. The NBL reference case refers to simulation H500-$\Delta\theta$0-Γ0.

compensate for the limited thickening of the boundary layer. The vertical velocity fields shown in Figure 14(e-g) clearly illustrate that the upward motion caused by these waves propagates down to turbine-hub height, generating patches of low and high wind speed. According to Equation 5.1, the interfacial-wave wavelength is 6.1 km and 4 km for cases H500-$\Delta\theta$5-Γ1 and H500-$\Delta\theta$8-Γ1, which is in line with the 7.3 km and 4.9 km observed in Figure 14(f,g). However, λ_x measures 10.1 km for case H500-$\Delta\theta$2-Γ1, which corresponds to 2/3 of the farm length. For this case, interfacial waves are not visible in Figure 14(a,e,i). We speculate that a longer domain is necessary for these waves to become clearly visible. We also remark the presence of a V-shape pattern at the farm sides, which is very similar to the one noted by Allaerts & Meyers (2019). This phenomenon will be further discussed in Section 5.3.

Finally, Figure 14(g-i) displays pressure perturbation with respect to the inflow value. The footprint of the counteracting pressure gradient in the farm induction region together with the favourable one across the farm is positively correlated with $\Delta\theta$. However, case H500-$\Delta\theta$5-Γ4 shows the highest pressure perturbation magnitude, the latter being roughly 1.5 times the one obtained in case H500-$\Delta\theta$2-Γ1. We speculate that this is due to the chocking effect (Smith 2010), since $Fr = 0.99$ in this case. Moreover, the V-shape pattern causes a favourable pressure gradient also at the farm sides, which further enhances the channelling effects. We note that the recycling of pressure perturbations along the spanwise direction suggests that the domain width should be further increased in future studies. Finally, Figure 14(d,h,l) shows the results obtained in the NBL reference case. As mentioned earlier, the pressure perturbations are at least one order of magnitude lower than in cases with thermal stratification above the ABL. This explains the absence of
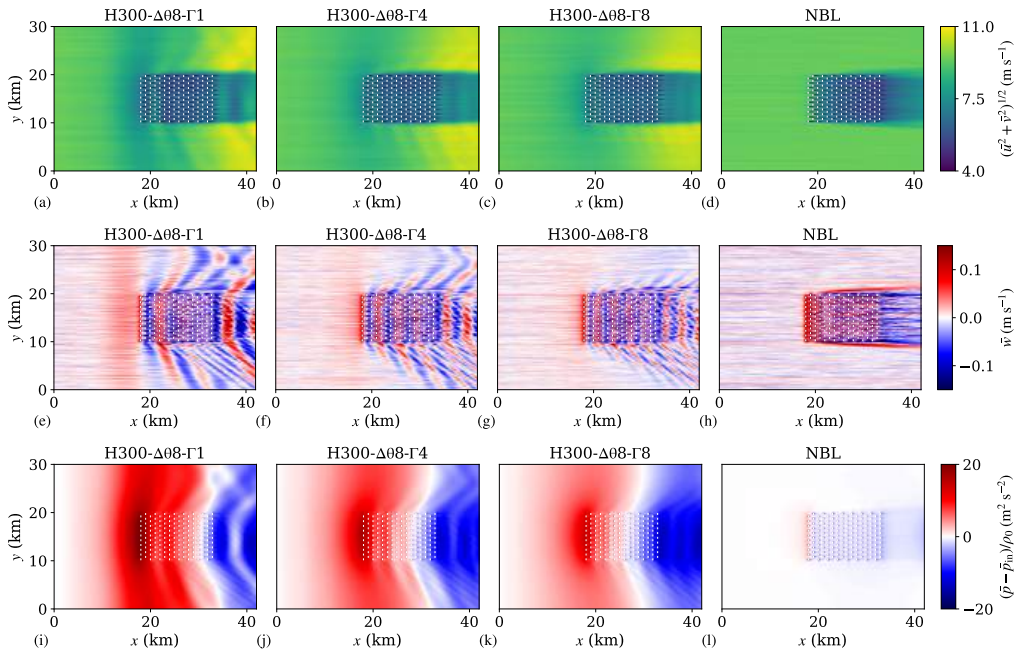
FIGURE 15. Contours of the time-averaged (a-d) velocity magnitude, (e-h) vertical velocity and (i-l) pressure perturbation in an x–y plane taken at turbine-hub height for cases (a,e,i) H300-$\Delta\theta$8-Γ1, (b,f,j) H300-$\Delta\theta$8-Γ4, (c,g,k) H300-$\Delta\theta$8-Γ8 and (d,h,l) the NBL reference case. The location of the turbine-rotor disks is indicated with vertical white lines. The NBL reference case refers to simulation H500-$\Delta\theta$0-Γ0.

velocity reductions several kilometers upstream of the farm together with a monotonic decrease in velocity magnitude between the first- and last-row turbines.

We now turn our attention to the effects of changes in the free-atmosphere lapse rate. Equation 5.1 shows that the interfacial-wave horizontal wavelength is negatively correlated with the Brunt–Väisälä frequency. This means that an increases in free-atmosphere stability results in a lower λ_x value. Figure 15 clearly illustrates this behaviour. As Γ increases, air parcels find more resistance in displacements along the vertical direction due to the stronger buoyant forces. Therefore, a stronger free-lapse rate damps waves along the inversion layer, limiting its vertical displacement. Consequently, a lower cold anomaly is generated, which leads to lower pressure perturbations. This is visible when comparing Figure 15(i,k) which shows x–y planes of pressure perturbations at turbine-hub height obtained with $\Gamma = 1$ K km^{-1} and $\Gamma = 8$ K km^{-1}, respectively, while keeping all other parameters constant. This also implies that the hydrostatic flow blockage effect reduces as the stability of the free-atmosphere increases in the presence of a strong capping-inversion strength, as shown in Figure 15(a-c). This result is in contrast with findings of Abkar & Porté-Agel (2013) and Wu & Porté-Agel (2017), who observed that changing the free-lapse rate from 1 K km^{-1} to 10 K km^{-1} caused a power drop of about 35%. However, in their study, they were at the same time varying the capping-inversion height and strength, which explains this difference in power output. Finally, Figure 15(e-g) shows the vertical velocity fields, where the V-shape pattern at the farm sides together with interfacial-wave effects are clearly visible. Interestingly, we also observe slanted lines at the left side of the farm with an angle of 29° with respect to the streamwise direction. We note that this effect is related to the perturbation introduced by the single turbines
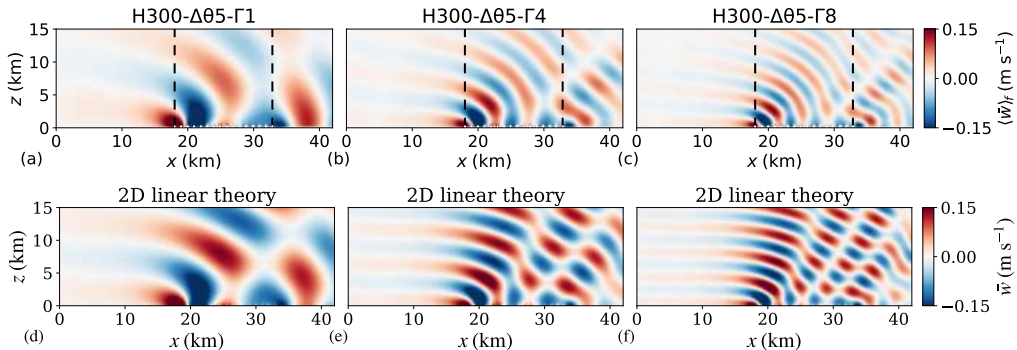
FIGURE 16. Contours of the time-averaged vertical velocity field in an x–z plane further averaged along the farm width for cases (a) H300-$\Delta\theta5$-$\Gamma1$, (b) H300-$\Delta\theta5$-$\Gamma4$ and (c) H300-$\Delta\theta5$-$\Gamma8$. (d-f) Vertical velocity field obtained with the two-dimensional gravity-wave linear-theory model described in Appendix B. For instance, the internal waves in panel (d) are excited by an obstacle with shape given by the capping-inversion vertical displacement obtained in case H300-$\Delta\theta5$-$\Gamma1$. The vertical black dashed lines in panel (a-c) denote the location of the first- and last-row turbines while the location of the turbine-rotor disks in panels (a-c) are indicated with vertical white lines.

and will be further discussed in Section 5.3. For the sake of comparison, we report again the results obtained for the NBL reference case in Figure 15(d,h,l).

5.3. *Comparison between LES results and gravity-wave linear-theory models*

The simplicity of gravity-wave linear-theory models contributed to their spread in analyzing mountain-wave phenomena. A wide variety of this type of models can be found in Gill (1982), Nappo (2002), Lin (2007), Sutherland (2010) and Teixeira (2014). More recently, the same theory has been applied to wind-farm studies, since the latter can be considered as a "permeable mountain". Example of these models can be found in Smith (2010), Allaerts & Meyers (2018), Allaerts & Meyers (2019), Devesse *et al.* (2022) and Smith (2022, 2023). In the current section, we perform a comparison of our results against some of the simplest wind-farm gravity-wave linear-theory models.

Figure 16 compares the internal gravity-wave pattern obtained in three LESs against the results obtained with a simple two-dimensional gravity-wave linear-theory model (Nappo 2002). The latter is a quasi-analytical model which takes as an input the shape of the obstacle, assumed impermeable, which is given to the system of equations as a bottom boundary conditions. In the current study, the inversion-layer displacement shown in Figure 19(a-d) defines the obstacle shape. For the sake of clearness, we briefly explain this linear model in Appendix B. We remark the excellent agreement between our results and linear theory, particularly in terms of gravity-wave phase line and vertical wavelength. Moreover, the slanted region tilted downstream of zero vertical velocity that forms near the trailing edge of the farm is captured by both models. This supports the idea that this phenomenon is not a manifestation of internal gravity-wave reflection but is rather due to the interaction between two out-of-phase trains of internal waves triggered by the first- and last-row turbines – see Figure 4. We believe that this good comparison is mostly a result of the effort spent in properly developing and calibrating the buffer regions in the main domain. We note that a discussion on the internal gravity-wave reflectivity is reported in Appendix C.

Next, Figure 17 displays a x–y plane of the time-averaged vertical velocity field taken at turbine-tip height for case H300-$\Delta\theta5$-$\Gamma1$. The flow deceleration causes a strong upward
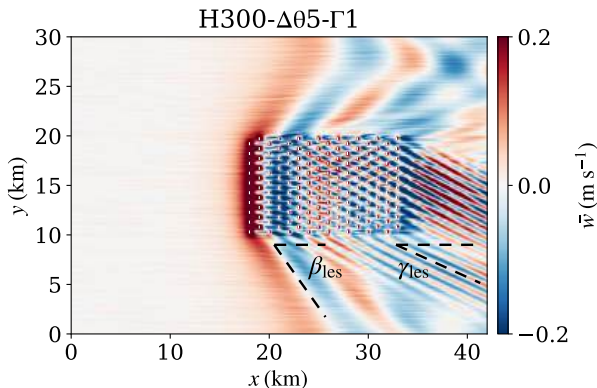
FIGURE 17. Contours of the time-averaged vertical velocity field in an x–y plane taken at turbine-tip height for case H300-$\Delta\theta5$-$\Gamma1$. The definition of the farm V-shape angle β_{les} together with the angle that the slanted lines make with the horizontal γ_{les} are reported in the figure. The location of the turbine-rotor disks is indicated with vertical white lines.

motion in the proximity of the first rows of turbines, which results in interfacial waves along the capping inversion. The upward and downward motion that these waves generate is very visible in Figure 17, both in and around the farm.

Two additional distinct phenomena take place. First, we observe a V-shape pattern around the farm which has been already observed and investigated by Allaerts & Meyers (2019). They reported that the angle of the pair of characteristic lines which gives rise to this pattern is only dependent on the Froude number and is given by

$$\beta_{\text{lin}} = \arctan\left(\left(Fr^2 - 1\right)^{-1/2}\right), \tag{5.2}$$

where the Froude number is defined as a ratio between a boundary-layer velocity scale (i.e. U_B) and the interfacial-wave phase speed. In shallow-water wave theory, the phase speed is given by $\sqrt{g'H}$ (Acheson 1990; Sutherland 2010). This theory holds under the assumption that $L > 4\pi H$, where L denotes the length scale of the forcing. If we use the distance between first- and last-row turbines as a length scale (i.e. $L = L_x^f$), this relation holds and the Froude number is therefore defined as $Fr = U_B/\sqrt{g'H}$ (Smith 2010; Allaerts & Meyers 2019). For instance, the Froude number is 1.29 for the case shown in Figure 17, which results in $\beta_{\text{lin}} = 50.8°$. This value is in excellent agreement with the one observed in the LES results, which measures $\beta_{\text{les}} = 51°$. Equation 5.2 shows that the angle is well defined only for supercritical flows. In subcritical cases, the characteristic lines become imaginary and no V-shape pattern occurs around the farm (Allaerts & Meyers 2019). The second pattern observed in Figure 17 is a set of slanted lines, and is related to the perturbation introduced by the turbine spacing. In fact, if we use as a length scale the equivalent turbine spacing $S_e = D\sqrt{s_x s_y}$, then we should define the interfacial-wave phase speed using deep-water wave theory, which holds when $L < H/\pi$. Using this theory, the Froude number is defined as

$$Fr_{dw} = \frac{U_B}{\sqrt{\dfrac{g' S_e}{2\pi}\tanh\left(\dfrac{2\pi H}{S_e}\right)}}$$

where the denominator represents the interfacial-wave phase speed. This Froude number measures 1.88 for case H300-$\Delta\theta5$-$\Gamma1$. Using Equation 5.2, this results in an angle of 32.1°,
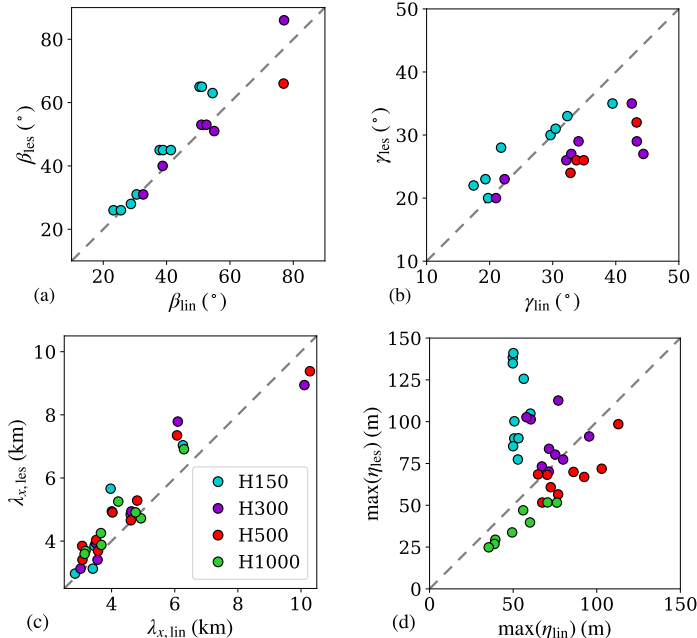
FIGURE 18. (a,b) Comparison of the β and γ angles measured in the LES results against the values predicted by linear theory (Allaerts & Meyers 2019). (c) Comparison of trapped-wave horizontal wavelength between LES results and the linear theory model of Vosper (2004) and Sachsperger *et al.* (2015). (d) Comparison of maximum inversion-layer vertical displacement between the LES results and the one-dimensional linear model developed by Allaerts & Meyers (2018).

which we denote with γ_{lin}. Also, this angle is in good agreement with the one observed in the LES results, which measures $\gamma_{\text{les}} = 28°$. We note that the lines that make the angles β_{les} and γ_{les} with the horizontal are also reported in Figure 17. While the angle is explained by Equation 5.2, we also see in Figure 17 that these slanted lines only propagate along the left side of the farm. We speculate that this is due to the asymmetry generated by the Coriolis force.

The angles β_{les} and γ_{les} are measured by carefully aligning a slanted line to the pattern observed in the vertical velocity field, as shown in Figure 17. A comparison between the β_{lin} and β_{les} angles for supercritical flows is shown in Figure 18(a). Overall, we observe an excellent agreement, with values collapsing along the diagonal. Next, Figure 18(b) compares the angle formed by the slanted lines triggered by the turbine spacing. We see again a good agreement, with γ_{les} slightly lower than γ_{lin} in deeper boundary layers. Finally, Figure 18(c) shows a comparison between the interfacial-wave horizontal wavelength obtained in LES against the one evaluated with linear theory, i.e. using Equation 5.1.

Allaerts & Meyers (2018) derived a linear one-dimensional model for the capping-inversion vertical displacement in response to a drag force imposed within the whole ABL. The governing equation reads as

$$\left(1 - \frac{1}{Fr^2}\right)\frac{\partial \eta}{\partial x} = c_t \Pi(x) - 2\big(c_t \Pi(x) + c_d\big)\frac{\eta}{H} - \frac{1}{P_N}\mathcal{G}_N(\eta), \qquad (5.3)$$

where $\Pi(x)$ denotes a step function with support going from the start to the end of the

farm and $c_d = u_\star/U_B$ represents the friction with the ground. Moreover, the thrust force imposed on the flow scales linearly with c_t, which is defined as

$$c_t = \frac{1}{2}\frac{\pi C_T}{4 s_x s_y}\eta_w \gamma_v \tag{5.4}$$

with γ_v a wind-profile shape factor determined using the precursor flow field and η_w the wake efficiency. Finally, $\mathcal{G}_N(\eta)$ is a linear operator that accounts for internal-wave effects and is expressed as

$$\mathcal{G}_N(\eta) = \frac{1}{2\pi}\int |k|\left(\int \eta(x')e^{-ikx'}dx'\right)e^{ikx}dk. \tag{5.5}$$

We refer to Appendix 2 in Allaerts & Meyers (2018) for a full derivation of Equation 5.3. Given the atmospheric state, Equation 5.3 predicts the capping-inversion displacement along the streamwise direction. Further, we name the maximum inversion-layer vertical displacement obtained with Equation 5.3 and with the LES results as $\max(\eta_{\mathrm{lin}})$ and $\max(\eta_{\mathrm{les}})$, respectively. These two quantities are displayed in Figure 18(d), which shows a good match except for cases H150, for which $\max(\eta_{\mathrm{lin}}) < \max(\eta_{\mathrm{les}})$. We note that the values of η_w, β_{les}, γ_{les}, $\lambda_{x,\mathrm{les}}$ and $\max(\eta_{\mathrm{les}})$ for all cases are summarized in Table 5.6.

In this section, we have seen that our results match well when compared against various gravity-wave linear-theory models found in the literature. This further confirms that the LES results are not distorted by the domain boundaries and provide an interesting benchmark for the development, validation and calibration of existing and future low- and medium-fidelity wind-farm models.

5.4. *Comparison of flow profiles*

We now investigate and compare flow profiles among all cases. Results are reported in Figure 19, which displays time-averaged flow profiles as a function of the streamwise direction. We start the analysis with Figure 19(a-d) which displays the streamwise variation of vertical inversion-layer displacement, here denoted with η, further averaged along the farm width. For the CNBL cases, η is defined as the difference between the capping-inversion top evaluated in precursor and main domains using the Rampanelli & Zardi (2004) model. It is interesting to see that in the presence of free-atmosphere stratification, the flow reacts to the presence of the farm several kilometers upstream. Cases with a weak inversion layer show higher displacements, independently from the inversion-layer height. This is due to the weak resistance to vertical motion that air parcels have in such cases. As $\Delta\theta$ increases, interfacial waves with a lower wavelength get excited within the farm and in its wake. As noted previously, a stronger free atmosphere limits the displacement of the inversion layer, particularly within the first couple of turbine rows. Overall, shallow boundary layers tend to show higher inversion-layer vertical displacements than deeper ones. Moreover, η sharply decreases downwind the last row of turbines in all cases, as a response to the flow acceleration in the wind-farm wake. In the NBL reference case, the absence of free-atmosphere stratification allows for higher growth of the ABL. In this case, η, which is computed as a streamline, shows a monotonic growth across the farm, with a maximum displacement obtained at the last-row turbine location.

Perturbations in the potential-temperature field are shown in Figure 19(e-f), averaged within the capping inversion height and along the farm width. As H increases, the cold anomaly reduces in magnitude. For instance, the minimum negative temperature perturbation is -1.4 K for the H1000 cases, while it attains a value of -4.6 K in the H150 ones. Even when the inversion-layer displacement is limited by high $\Delta\theta$ values, the
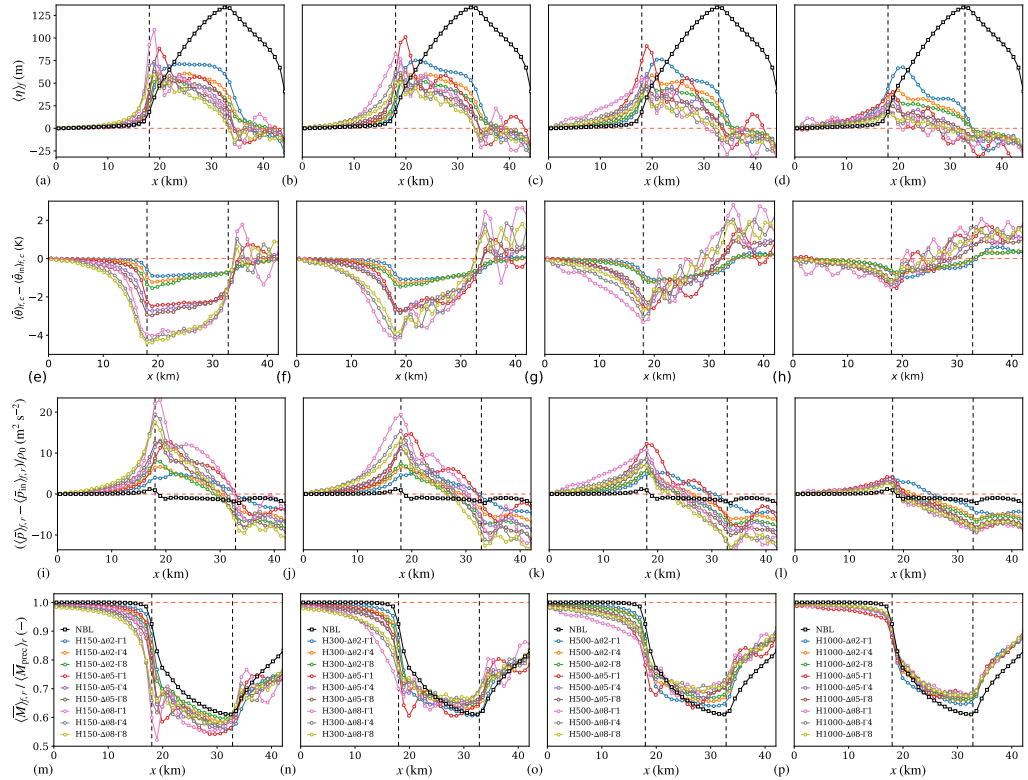
FIGURE 19. Time-averaged (a-d) capping-inversion displacement, (e-h) potential-temperature perturbation, (i-l) pressure perturbation and (m-p) velocity magnitude averaged over the farm width as a function of the streamwise direction. The potential-temperature perturbation is further averaged over the capping-inversion thickness, while the other quantities are averaged over the turbine-rotor height. Moreover, the cases are organized per capping-inversion height. The vertical dashed black lines denote the location of the first- and last-row turbines.

strong inversion that characterizes such cases generates higher temperature differences, which translate into stronger pressure perturbations. The latter are shown in Figure 19(i-l), averaged along the farm width and within the turbine-rotor height. Here, we observe that the cases with strong unfavourable and favourable pressure gradients are the ones with a strong inversion layer. For instance, the counteracting pressure gradient in case H300-$\Delta\theta$8-Γ1 is 4.4 times the one obtained in case H300-$\Delta\theta$2-Γ1. Pressure feedbacks in the neutral reference case are negligible when compared to the ones obtained in the CNBL cases. For instance, case H300-$\Delta\theta$5-Γ4, which Figure 2 defines as a highly probable atmospheric state over the North Sea, has a 14 times stronger unfavourable pressure gradient than the NBL reference case. However, we should note that all stratified cases are also characterized by a favourable pressure gradient through the farm, while the NBL reference case does not show this feature.

The pressure-perturbation effects on the velocity magnitude are evident in Figure 19(m-p). The NBL reference case shows a reduction in wind speed only several rotor diameters upstream of the farm. Consequently, the velocity at the first-row turbine location is always higher than in the cases with thermal stratification above the ABL. Interestingly, the vertical motion generated by the interfacial waves in the CNBL cases has direct consequences in terms of velocity magnitude at the turbine-hub height. For instance, the velocity magnitude at the fourth-row turbine location is 5%
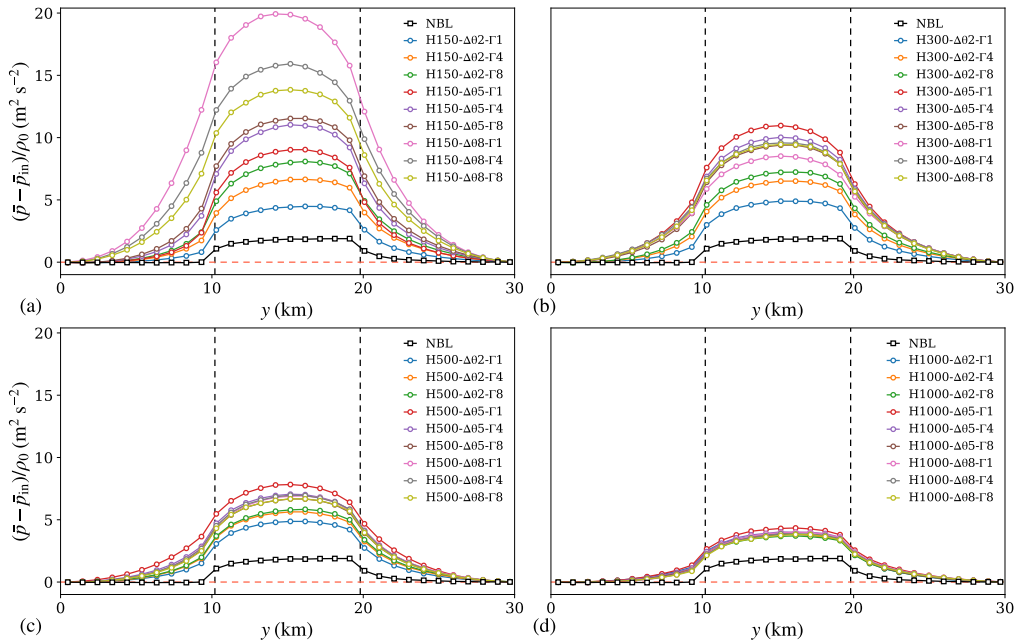
FIGURE 20. Pressure perturbation as a function of the domain width taken at $x = 18$ km (i.e. the location of the first-row turbines) and further averaged over the turbine-rotor height for cases (a) H150, (b) H300, (c) H500 and (d) H1000. The vertical dashed black lines denote the location of the first- and last-column turbines.

higher than the one measured at the farm leading edge for case H300-$\Delta\theta8$-$\Gamma1$. As H increases, the flow response becomes less sensitive to changes in $\Delta\theta$ and Γ. In fact, as the inversion-layer height approaches the equilibrium height of the TNBL, its effects on the farm–ABL interactions become smaller. Consequently, the velocity profiles and pressure perturbation of the CNBL cases get closer to the ones of the NBL reference case, as shown in Figure 19(l,p). We remark that a stronger blockage effect and velocity deficits in shallow boundary layers have been observed also in SCADA data from the Nordsee Ost and Amrumbank West wind farms located in the German Bight area Cañadillas *et al.* (2023) and in a previous study (Allaerts & Meyers 2017).

Cases H500-$\Delta\theta8$-$\Gamma4$, H1000-$\Delta\theta8$-$\Gamma1$ and H1000-$\Delta\theta8$-$\Gamma4$ in particular show oscillations in the capping-inversion displacement and temperature perturbation already in the farm induction region. Most likely, these are spurious effects introduced by the fringe region. In fact, Lanzilao & Meyers (2023) have shown that their wave-free fringe-region technique can still introduce some perturbations in the domain of interest for a combination of low Fr and P_N numbers, which characterize these three cases – see Table 1.

Finally, Figure 20 focuses on the pressure build-up measured at the first-row turbine location along the spanwise direction. Here, the inverse relationship between capping-inversion height and counteracting pressure gradient is evident. Moreover, a deep boundary layer makes the simulation quasi-independent of changes in $\Delta\theta$ and Γ, as all profiles collapse in Figure 20(d). However, the pressure build-up in all CNBL cases still remains higher than the one attained in the NBL reference case. Figure 20 also shows that turbines situated in the centre of the farm experience a higher counteracting pressure gradient than those located at the farm sides. The asymmetry of the profiles with respect to the domain centerline is caused by the presence of the Ekman layer.
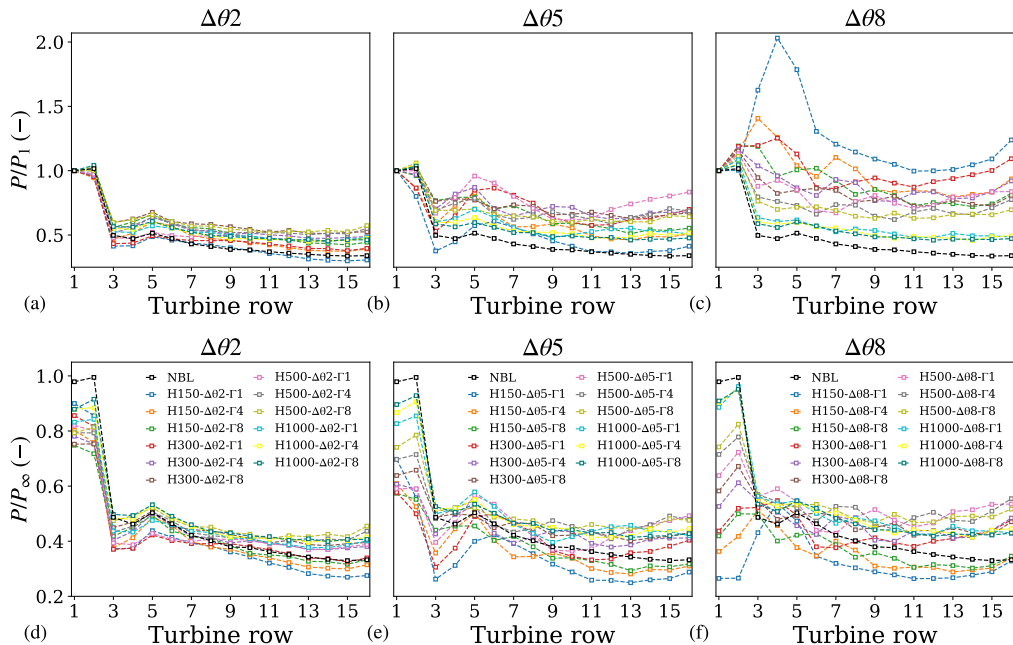
FIGURE 21. Averaged power output per turbine row normalized by (a-c) P_1 of the respective simulation and (d-f) P_∞ of the respective inversion-layer height obtained with a capping-inversion strength of (a,d) $\Delta\theta = 2$ K, (b,e) $\Delta\theta = 5$ K and (c,f) $\Delta\theta = 8$ K under different inversion-layer heights and free-atmosphere lapse rates. Here, P_1 denotes the averaged power outputs of first-row turbines while P_∞ represents the power output of a turbine operating in isolation obtained with the single-turbine simulations – see Appendix A.

5.5. *Wind-farm power production*

The time- and row-averaged turbine power output normalized with the first-row turbine power is displayed in Figure 21 organized per capping-inversion strength. A very similar trend in power output is observed for cases with weak inversion-layer strengths, as shown in Figure 21(a). The farm has a staggered layout, therefore the high-speed channels that form between the turbines in the first row allow for a slightly higher power generation at the second row (McTavish *et al.* 2015; Meyer Forsting *et al.* 2017). After a drop of about 50% between the 2nd and 3rd row, the power remains approximately constant, with a minor increase towards the farm trailing edge for the cases with thermal stratification above the ABL. As the inversion-layer strength increases, power fluctuations are observed within the farm. These are mostly caused by the vertical motion generated by interfacial waves. Consequently, the power doesn't show a monotonic trend across the farm. Instead, the 5th row often extracts more power than the 3rd one when $\Delta\theta = 5$ K, with differences up to 40%. A more extreme behaviour is observed in Figure 21(c), where in three cases a waked row extracts more power than the first row. Moreover, the strong favourable pressure gradient that develops across the farm in cases with a strong inversion layer also leads to an increase in power production towards the end of the farm. This phenomenon is accentuated in shallow boundary layers. For instance, the difference in power output between first- and last-row turbines is only about 8% in case H300-$\Delta\theta$8-Γ4, while the last-row turbines produce 23% more power than the first one in case H150-$\Delta\theta$8-Γ1.

Figure 21(d-e) shows the same results but normalized with P_∞, that is the power
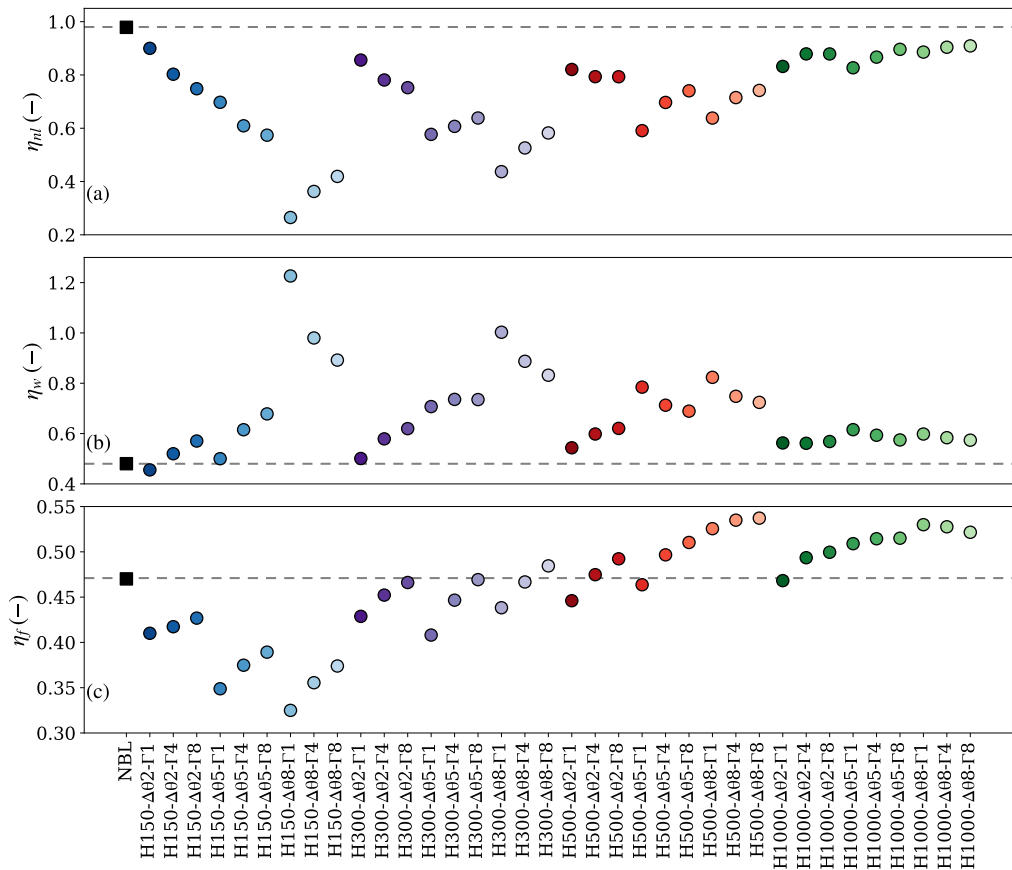
FIGURE 22. (a) Non-local, (b) wake and (c) farm efficiency as a function of all simulation cases. The cases with thermal stratification above the ABL are represented by a circle while the NBL reference case is marked with a square. The horizontal grey dashed line indicates the relative efficiency value obtained in the NBL reference case.

output of a turbine operating in isolation. In the CNBL cases, the ratio P_1/P_∞ (i.e. the non-local efficiency) is always much lower than 1, with a minimum of 0.26 attained in case H150-$\Delta\theta$8-Γ1. Moreover, the flow-blockage effect is much more sensitive to the inversion-layer height in the presence of strong capping inversion, as shown in Figure 21(f). In the neutral reference case, $P_1/P_\infty \approx 1$. Once more, this suggests that the flow deceleration in the farm induction region is mostly related to atmospheric gravity waves. Moreover, the power output keeps decreasing towards the farm trailing edge in the NBL reference case, while a power increase is observed for the majority of the CNBL cases. This is due to the favourable pressure gradient acting as an energy source across the farm.

5.6. *Wind-farm efficiencies*

We now turn our attention to the wind-farm efficiency, as well as the non-local and wake efficiencies, which are illustrated in Figure 22 for all cases. We note that these efficiencies are defined in Equation 4.1. Figure 22(a) shows that the strong counteracting pressure gradient that characterizes shallow boundary layers causes η_{nl} to be lower in the H150 cases than in the H1000 ones. The highest non-local efficiency is attained in the NBL reference case, showing that the cumulative turbine induction has a minor
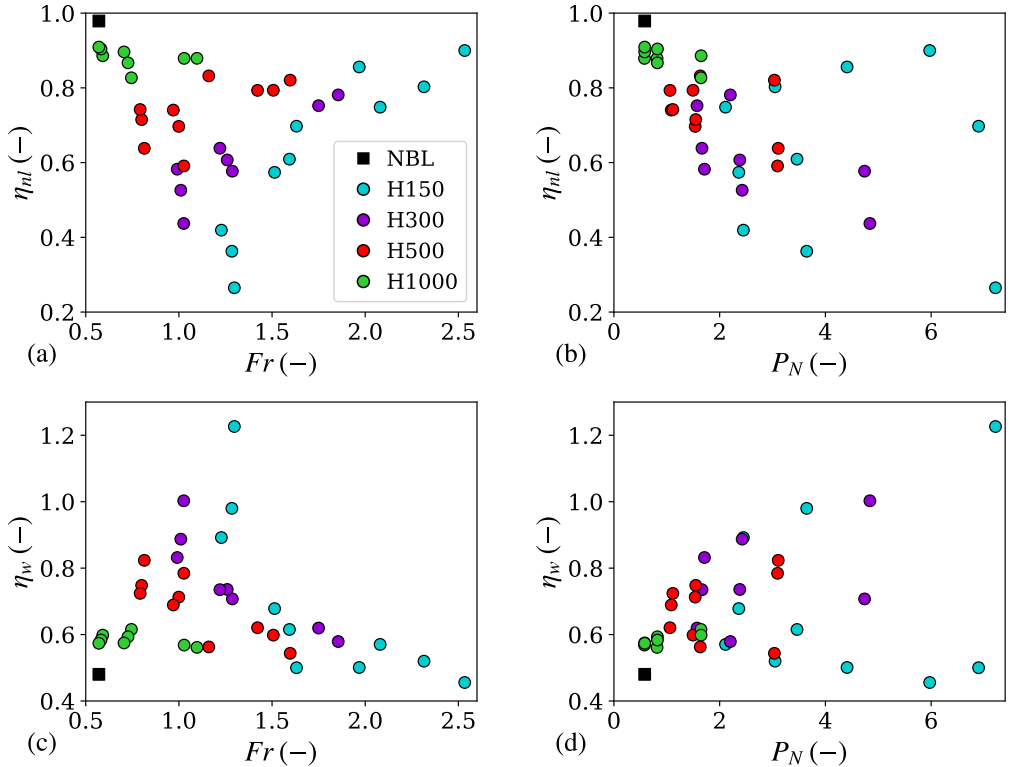
FIGURE 23. (a,b) Non-local and (c,d) wake efficiency as a function of the (a,c) Fr and (b,d) P_N numbers.

contribution to the flow-blockage effect for this case. The wake efficiency is shown in Figure 22(b). As hypothesized by Allaerts & Meyers (2018), a low non-local efficiency leads to a higher wake efficiency. In fact, the accumulation of potential energy caused by the flow slow-down in front of the farm is converted back into kinetic energy which accelerates the flow across the farm (Allaerts & Meyers 2018). This negative correlation is clearly visible when comparing results in Figure 22(a,b). We note that case H150-$\Delta\theta$8-Γ1 has a wake efficiency greater than 1. For this atmospheric condition, the average power generated by the waked rows is higher than the one extracted by first-row turbines. The absence of favourable pressure gradients across the farm causes the wake efficiency of the NBL reference case to be among the lowest. Finally, Figure 22(c) displays the overall farm efficiency. The farm efficiency in the H150 and H300 cases is lower than the NBL reference case, while becomes higher for the H500 and H1000 cases, showing the strong influence that the capping-inversion height has on the wind-farm power output. Moreover, we observe that the farm efficiency is positively related with Γ. In fact, a free atmosphere with strong stratification leads to a higher wind-farm power output than a weakly stratified atmosphere, for a fixed H and $\Delta\theta$ value. We note that the error bars representing the 95% confidence interval computed with the moving block bootstrapping method for all efficiencies are in the order of $\pm 1\%$ and for this reason are not shown in Figure 22.

Next, we investigate how the non-local and wake efficiencies scale with the atmospheric state. In a first attempt, we plot the efficiencies against the Fr and P_N numbers, which are the two non-dimensional groups that govern gravity-wave effects. Results are shown in
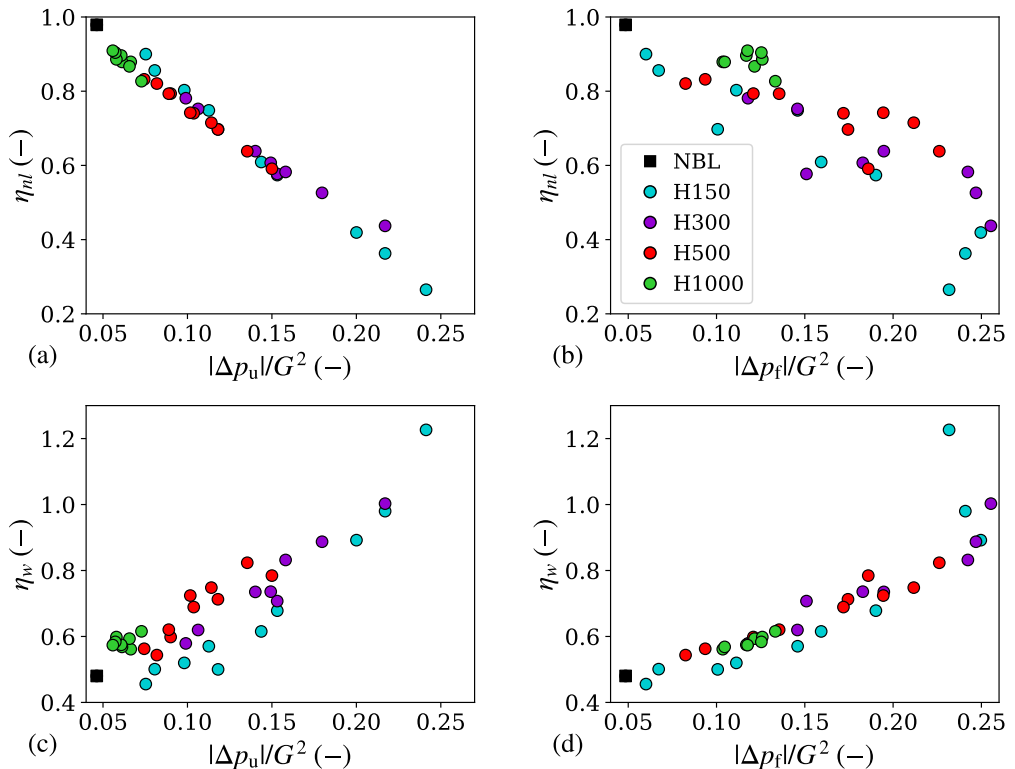
FIGURE 24. (a,b) Non-local and (c,d) wake efficiency as a function of the (a,c) unfavourable and (b,d) favourable pressure gradients magnitude normalized by the geostrophic wind.

Figure 23. The lowest values of non-local efficiency are attained for $Fr \approx 1.3$. Figure 23(b) shows that in general, the non-local efficiency decreases as P_N increases. The wake efficiency shown in Figure 23(c,d) shows an opposite trend, as expected. Overall, values remain scattered along the parameter space and strong trends are not observed.

In the previous sections, we have seen that gravity-wave induced pressure gradients play a primary role in the flow dynamics. Therefore, in a second attempt, we try to scale the farm efficiencies against these pressure feedbacks. In particular, we define $\Delta p_u = \langle \bar{p} \rangle_{f,r}(x_{\text{ft}}) - \langle \bar{p} \rangle_{f,r}(x_{\text{in}})$ and $\Delta p_f = \langle \bar{p} \rangle_{f,r}(x_{\text{lt}}) - \langle \bar{p} \rangle_{f,r}(x_{\text{ft}})$ where $x_{\text{in}} = 0$ km represents the main domain inflow. Moreover, $x_{\text{ft}} = 18$ km and $x_{\text{lt}} = 32.85$ km denote the location of the first- and last-row turbines, respectively. Given this definition, Δp_u and Δp_f quantify the pressure feedback upstream and across the farm, respectively. Figure 24(a) shows the non-local efficiency as a function of Δp_u normalized by the geostrophic wind. Here, we can observe a very strong negative correlation. This is expected since the non-local efficiency quantifies the flow slow down in front of the farm, which depends on the magnitude of the unfavourable pressure gradient. An opposite trend is visible in Figure 24(d), where the wake efficiency shows a strong positive correlation with Δp_f, confirming the role of the favourable pressure gradient in accelerating the wake recovery mechanism.

Pressure perturbations induced by gravity waves scale with the capping-inversion vertical displacement η. In fact, Smith (2010) has shown that in Fourier domain

$$\frac{\hat{p}}{\rho_0} = \left(g \frac{\Delta\theta}{\theta_0} + \frac{i\left(N^2 - \Omega^2\right)}{m} \right) \hat{\eta}$$
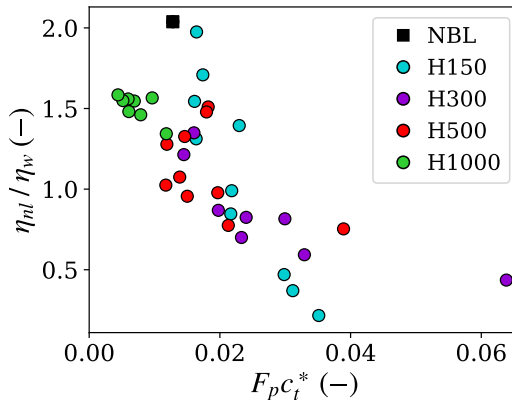
FIGURE 25. Ratio between the non-local and wake efficiency as a function of $F_p c_t^*$.

with m the vertical wave number and Ω the intrinsic wave frequency. Therefore, we believe that finding a good scaling parameter for η would also result in a scaling parameter for the efficiencies. A simple model that provides an estimate for η as a function of the atmospheric state has been proposed by Allaerts & Meyers (2018) and is reported in Equation 5.3. In the Fourier domain, this model reads as

$$\left(1 - Fr^{-2}\right)ik\hat{\eta} = c_t\widehat{\Pi} - \frac{2c_t}{H}\widehat{\Pi} * \hat{\eta} - 2c_d\frac{\hat{\eta}}{H} - P_N^{-1}|k|\hat{\eta} \tag{5.6}$$

where the operator $*$ denotes a convolution. The second and third terms on the right-hand side of Equation 5.6 represent a second-order term and the friction with the ground normalized with H, respectively, which are much smaller than the other terms. After neglecting these two terms, we can write

$$\hat{\eta} = \frac{c_t}{k}\left(P_N^{-1}\frac{|k|}{k} + i\left(1 - Fr^{-2}\right)\right)^{-1}\widehat{\Pi}. \tag{5.7}$$

Using the dominant wavelength $k_d = 2\pi/L_x^f$ in the streamwise direction, we define the following non-dimensional group

$$F_p \triangleq \frac{k_d}{c_t\|\widehat{\Pi}(k_d)\|}\|\hat{\eta}(k_d)\| = \left(P_N^{-2} + \left(1 - Fr^{-2}\right)^2\right)^{-0.5} \tag{5.8}$$

where $\|\widehat{\Pi}(k_d)\|$ and k_d are constant values since we do not vary the farm layout. By defining $c_t = c_t^*\eta_w$, we find that $\|\hat{\eta}(k_d)\|$ scales with $F_p c_t^*\eta_w$. We have previously shown that η_{nl} is strongly related to Δp_u, which in turn depends upon the vertical displacement of the capping inversion. Hence

$$\eta_{nl} \propto \Delta p_u \propto \|\hat{\eta}(k_d)\| \propto F_p c_t^*\eta_w \tag{5.9}$$

implying that η_{nl}/η_w scales with $F_p c_t^*$. Figure 25 confirms this result, showing a relatively strong negative correlation. We note that the value of η_{nl}, η_w and η_f together with P_1, P_∞, Δp_u and Δp_f for all cases are summarized in Table 5.6.

6. Conclusions

This study set out to analyze the flow response to wind-farm forcing under atmospheres with different thermal stratification above the ABL. To this end, we performed 40 LESs

Cases	β_{les}(°)	γ_{les}(°)	$\lambda_{x,les}$ (km)	$\max(\eta_{les})$ (m)	r(%)	η_{nl}(%)	η_w(%)	η_f(%)	P_1 (MW)	P_∞ (MW)	Δp_u (m²s⁻²)	Δp_f (m²s⁻²)
H150-Δ02-Γ1	26	22	-	138.3	2.57	90	46	41	7.06	7.84	7.53	6.01
H150-Δ02-Γ4	26	23	-	134.9	0.89	80	52	42	6.30	7.84	9.81	11.12
H150-Δ02-Γ8	28	28	-	141.0	0.58	75	57	43	5.87	7.84	11.26	14.59
H150-Δ05-Γ1	45	30	7.03	100.2	4.61	70	50	35	5.47	7.84	11.81	10.07
H150-Δ05-Γ4	45	31	4.85	90.0	1.78	61	62	37	4.78	7.84	14.37	15.93
H150-Δ05-Γ8	45	33	3.13	85.4	1.12	57	68	39	4.50	7.84	15.32	19.02
H150-Δ08-Γ1	65	35	5.66	125.6	8.06	26	123	32	2.08	7.84	24.13	23.17
H150-Δ08-Γ4	65	-	3.85	90.1	2.59	36	98	36	2.85	7.84	21.70	24.09
H150-Δ08-Γ8	63	-	2.97	77.4	1.58	42	89	37	3.29	7.84	20.01	24.97
H300-Δ02-Γ1	31	20	-	104.8	3.33	86	50	43	6.85	8.00	8.06	6.72
H300-Δ02-Γ4	31	20	-	101.4	0.82	78	58	45	6.25	8.00	9.90	11.78
H300-Δ02-Γ8	-	23	-	102.7	0.49	75	62	47	6.02	8.00	10.63	14.58
H300-Δ05-Γ1	53	26	7.79	112.6	7.56	58	71	41	4.62	8.00	15.31	15.09
H300-Δ05-Γ4	53	27	4.94	83.8	1.92	61	74	45	4.86	8.00	14.93	18.28
H300-Δ05-Γ8	51	29	3.41	73.2	1.13	64	74	47	5.11	8.00	14.02	19.47
H300-Δ08-Γ1	86	35	4.94	91.2	7.17	44	100	44	3.50	8.00	21.70	25.54
H300-Δ08-Γ4	-	29	3.94	77.4	3.75	53	89	47	4.21	8.00	17.97	24.69
H300-Δ08-Γ8	-	27	3.13	70.1	2.84	58	83	48	4.66	8.00	15.81	24.23
H500-Δ02-Γ1	40	-	8.94	80.3	3.39	82	54	45	6.49	7.90	8.19	8.25
H500-Δ02-Γ4	-	-	5.28	68.2	0.72	79	60	47	6.28	7.90	9.00	12.09
H500-Δ02-Γ8	-	-	3.85	68.5	0.41	79	62	49	6.27	7.90	8.89	13.55
H500-Δ05-Γ1	66	24	7.35	98.5	7.77	59	78	46	4.67	7.90	15.00	18.59
H500-Δ05-Γ4	62	26	4.66	69.9	2.26	70	71	50	5.51	7.90	11.80	17.44
H500-Δ05-Γ8	-	26	3.69	60.8	0.97	74	69	51	5.86	7.90	10.37	17.19
H500-Δ08-Γ1	70	32	4.91	66.9	8.75	64	82	53	5.05	7.90	13.54	22.62
H500-Δ08-Γ4	70	-	4.03	56.5	5.49	72	75	53	5.66	7.90	11.41	21.17
H500-Δ08-Γ8	-	-	3.41	51.6	4.98	74	72	54	5.87	7.90	10.17	19.44
H1000-Δ02-Γ1	-	-	9.38	71.8	3.20	83	56	47	6.34	7.62	7.44	9.36
H1000-Δ02-Γ4	-	-	4.72	51.7	0.63	88	56	49	6.70	7.62	6.64	10.35
H1000-Δ02-Γ8	-	-	3.69	47.0	0.55	88	57	50	6.70	7.62	6.12	10.46
H1000-Δ05-Γ1	-	-	6.91	51.6	11.54	83	62	51	6.30	7.62	7.28	13.33
H1000-Δ05-Γ4	-	-	4.91	39.7	3.53	87	59	51	6.61	7.62	6.57	12.15
H1000-Δ05-Γ8	-	-	3.88	33.7	0.77	90	57	52	6.83	7.62	6.08	11.69
H1000-Δ08-Γ1	-	-	5.25	29.4	15.82	89	60	53	6.75	7.62	5.79	12.59
H1000-Δ08-Γ4	-	-	4.25	26.9	8.87	90	58	53	6.89	7.62	5.73	12.54
H1000-Δ08-Γ8	-	-	3.60	24.8	5.96	91	57	52	6.93	7.62	5.58	11.76
NBL	-	-	-	-	-	98	48	47	7.74	7.90	4.63	4.85

TABLE 3. Overview of the simulation results including the farm V-shape angle β_{les}, the slanted lines angle γ_{les}, the trapped-wave horizontal wavelength $\lambda_{x,les}$, the maximum inversion-layer vertical displacement $\max(\eta_{les})$, the reflectivity r, the non-local efficiency η_{nl}, the wake efficiency η_w, the farm efficiency η_f, the first-row turbine power output P_1, the power output of a turbine operating in isolation P_∞ and the unfavourable and favourable pressure gradients magnitude Δp_u and Δp_f, respectively. We remark that the NBL reference case refers to simulation H500-Δθ0-Γ0.

of a 14.85×9.4 km^2 wind farm. Moreover, we run 21 additional LESs with varying domain sizes, with the aim of defining guidelines on how to select the domain length and width as a function of the inversion-layer height. The simulations were carried out with SP-Wind, an LES solver developed at KU Leuven. The main domain was driven by turbulent fully developed statistically steady flow fields obtained in precursor simulations. Moreover, the solver periodicity in the streamwise direction was broken using a wave-free fringe region technique while at the top of the domain an RDL was placed to damp gravity waves. Special effort in tuning the buffer regions was spent in order to minimize gravity-wave reflectivity and correctly impose the inflow conditions.

The sensitivity study to the domain size has shown that the wind-farm performance is quasi-independent of the induction-region length when using the wave-free fringe region technique. In fact, by varying the fetch between the main domain inflow and the first-row turbine from 10 km to 50 km, the non-local and wake efficiency only varied by about 1 percentage point, independently from the capping-inversion height. However, we observed more pronounced differences in the flow behaviour as the domain width was increased. For instance, the non-local efficiency obtained in a domain with a ratio L_y/L_y^f of 6.38 is 1.12 times the one measured in a domain with $L_y/L_y^f = 2.13$ for a shallow

boundary layer. Besides enhancing the flow-blockage effect, a domain with a low L_y/L_y^f ratio also increases the channelling effect at the farm sides. Therefore, we concluded that it is necessary to have a domain with a high L_y/L_y^f ratio when simulating wind-farm operations in shallow boundary-layer flows. Deeper boundary-layer flows are less sensitive to the domain width, but still require a wider space at the farm sides than simulations with a neutral atmosphere.

Next, we investigated the effect of changes in the capping-inversion height and strength, as well as free-atmosphere lapse rate, on the flow behaviour in and around the farm. In all cases, the flow convergence caused by the farm drag force displaces the capping inversion upward, creating a cold anomaly that induces pressure perturbations. We found very strong velocity deficits in shallow boundary layers, caused by the limited flow mixing and energy entrainment due to the close proximity of the inversion layer to the turbine-tip height. In turn, this resulted in higher inversion-layer vertical displacement and stronger cold anomalies. Therefore, shallow boundary-layer flows are characterized by a very strong counteracting pressure gradient in the farm induction region, further amplified by the presence of a strong inversion layer. Deeper boundary layers can accommodate the IBL growth, limiting flow redirection at the farm sides together with the vertical displacement of the capping inversion. Therefore, the counteracting pressure feedback has a lower magnitude in such cases. The pressure build-up in the farm entrance region is then released as a form of kinetic energy throughout the farm, which accelerates the wake recovery mechanism. This effect is more pronounced in shallow boundary layers. In regard to changes in $\Delta\theta$, we found that a stronger capping inversion reduces its vertical displacement, therefore increasing the flow rate at the farm sides. Moreover, inversion layers with higher strengths support interfacial waves with lower horizontal wavelengths. Finally, we noticed that a stronger free-atmosphere lapse rate limits air-parcel vertical motion, therefore reducing the magnitude of both the counteracting and favourable pressure gradients. We remark that the pressure perturbations in the NBL reference case were at least one order of magnitude lower than the ones in the CNBL cases.

The turbine power generation per row was also investigated. We observed that the flow divergence-convergence generated by interfacial waves causes considerable power fluctuations within the farm. Moreover, the turbine power tends to increase towards the farm trailing edge, particularly in cases with a shallow boundary layer and a high capping-inversion strength.

A non-local efficiency of 98% was observed for the NBL reference case. In contrast, the non-local efficiency attained values as low as 26% in the presence of thermal stratification above the ABL. This suggests that flow blockage is primarily related to atmospheric gravity waves. Moreover, we noticed that the non-local and wake efficiencies are inversely related. The farm efficiency in the H150 and H300 cases was lower than the NBL reference case, while it became higher for the H500 and H1000 cases. We also observed that the farm efficiency is positively related with Γ. In fact, a free atmosphere with strong stratification leads to a higher wind-farm power output than a weakly stratified atmosphere, for a fixed H and $\Delta\theta$ value. These observations suggested that the shape of the vertical potential-temperature profile has a significant impact on the wind-farm performance. Finally, we found no simple scaling between the efficiencies and the Fr and P_N numbers. Instead, a very good scaling was found with the pressure gradients. This observation allowed us to derive a new scaling parameter F_p for the ratio of non-local to wake efficiencies.

Finally, we compared our results against various one- and two-dimensional gravity-wave linear-theory models. Here, we noticed an excellent agreement between the internal gravity-wave pattern and magnitude, underlining the importance of properly calibrating

the fringe region and RDL. Moreover, the LES results were in line with linear theory also in terms of interfacial-wave horizontal wavelength and maximum inversion-layer vertical displacement.

The good agreement between gravity-wave linear-theory models and LES results and their consistency with previous findings entails that the numerical results are not distorted by the domain boundaries, and result in a valid benchmark for the development, validation and calibration of existing and future low- and medium-fidelity wind-farm models. In the future, we plan to extend the database to baroclinic atmospheres, where the geostrophic wind varies with height. Moreover, the presence of multiple capping inversions is also of interest. The farm geometry was kept constant in the current study, but we are aware that it can have significant effects on the flow behaviour. Therefore, pressure feedbacks under various farm layouts and densities will be investigated. Furthermore, we plan to study wind-farm operation in weak and strong SBLs, which are known to enhance the flow-blockage effect.

Declaration of interests

The authors report no conflict of interest.

Appendix A. Large-eddy simulation of a turbine operating in isolation

Single-turbine simulations are necessary to evaluate the power output of a turbine operating in isolation, which we define as P_∞. In the farm, first-row turbines are affected by flow blockage, so that their power output is naturally lower than P_∞. Moreover, Figure 3 illustrates that the turbulent statistically steady velocity profiles obtained with the precursor simulations are independent of the capping-inversion strength and free-atmosphere lapse rate. They only differ as H varies. Therefore, we perform only four single-turbine simulations, one per each value of H.

The presence of a single turbine allows us to use a much smaller domain, with an equal length and width of 10 km. This size corresponds to the one of the precursor domain. In the vertical direction, we keep $L_z = 25$ km as in the wind-farm simulations. The horizontal and vertical grid resolution also correspond to the ones adopted in the wind-farm simulations, meaning that we have 320, 460 and 490 points in the x, y and z-direction, respectively. The RDL and fringe region adopt the same setup described in Section 2.4. However, to account for the smaller domain, also the fringe region length has been reduced to 2.5 km compared to the 5.5 km adopted for the wind-farm simulations. Finally, the time horizon for the wind-farm start-up phase has been set to 1 h. Afterwards, statistics are collected over a simulation time of 1.5 h.
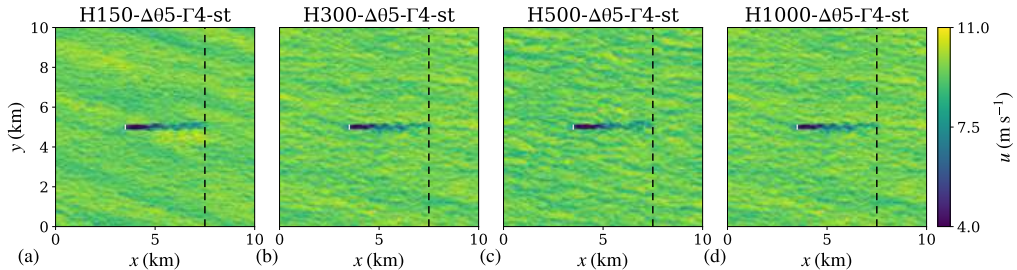
FIGURE 26. Contours of the instantaneous streamwise velocity field in an x-y plane taken at turbine-hub height for cases (a) H150-$\Delta\theta$5-Γ4-st, (b) H300-$\Delta\theta$5-Γ4-st, (c) H500-$\Delta\theta$5-Γ4-st and (d) H1000-$\Delta\theta$5-Γ4-st. The vertical black dashed line represents the start of the fringe region while the vertical white line denotes the turbine-rotor disk location.

Figure 26 illustrates instantaneous streamwise velocity fields in an x-y plane taken at turbine-hub height for the four single-turbine simulations. In all cases, we can easily distinguish the turbine wake, which recovers downwind before being fully replenished by the fringe-region body force, which restores the inflow conditions. Overall, we observe that the perturbations that the turbine induces on the flow are too small to excite any noticeable gravity-wave effects, such as flow blockage upstream and flow speed-up at its side. Consequently, we believe that this set of simulations is suitable for providing an estimate for P_∞. The free-stream power values are reported in Table 5.6.

Appendix B. A simple two-dimensional gravity-wave linear-theory model

We consider the Euler equations for irrotational, frictionless and adiabatic flow. Moreover, we neglect the Coriolis force and we assume that there is no variation in the y-direction, so that the problem can be considered to be two-dimensional. After manipulating the governing equations, the following solution in Fourier space for the streamwise and vertical velocity, pressure and potential temperature can be derived

$$\hat{u}(k,z) = -iGm\hat{h}_o e^{imz} \tag{B 1}$$

$$\hat{w}(k,z) = iGk\hat{h}_o e^{imz} \tag{B 2}$$

$$\hat{p}(k,z) = iG^2\rho_0 m\hat{h}_o e^{imz} \tag{B 3}$$

$$\hat{\theta}(k,z) = -\frac{N^2\theta_0}{g}\hat{h}_o e^{imz}, \tag{B 4}$$

where the hat denotes a variable in the Fourier domain, k represents the streamwise wavenumbers while i is the imaginary unit. Moreover, the vertical wavenumber m depends upon k and the atmospheric state, being defined as

$$m = \begin{cases} \sqrt{N^2/G^2 - k^2} & N^2/G^2 > k^2 \\ i\sqrt{k^2 - N^2/G^2} & N^2/G^2 < k^2 \end{cases}$$

where N is the Brunt–Väisälä frequency and G the geostrophic wind. We refer to Nappo (2002), Lin (2007), Sutherland (2010) and Cushman-Roisin & Beckers (2011) for more details on the derivation of Equations (B 1-B 4). The only input to the model consists of the obstacle shape in Fourier space, here denoted with $\hat{h}_o$. The latter is assumed impermeable. Moreover, it is assumed that the streamline slope equals the terrain slope
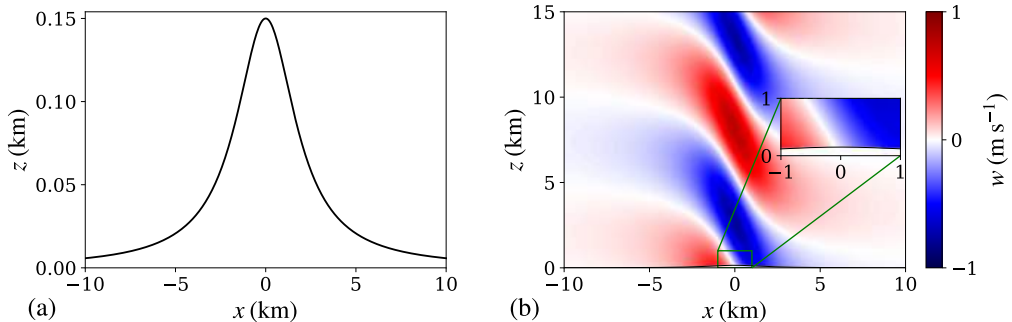
FIGURE 27. (a) Bell-shaped mountain known in the literature as the *Witch of Agnesi*. (b) Vertical velocity field predicted by the two-dimensional linear-theory model as a response to the obstacle shown in panel (a). In the center right of panel (b), the solution in the region close to the obstacle is magnified.

locally. Finally, an inverse Fourier transform is necessary to express Equation (B 1-B 4) in real space.

To conclude, we briefly show an example case. We consider a bell-shaped mountain, also known as the *Witch of Agnesi*. The latter is defined as

$$h_o(x) = \frac{h_m a^2}{x^2 + a^2}, \qquad \hat{h}_o(k) = \frac{h_m a}{2} e^{-ka} \quad \text{for} \quad k > 0,$$

where $h_m = 0.15$ km is the mountain height while $a = 2$ km denotes the mountain half-width. Moreover, we fix the geostrophic wind to 10 m s^{-1} and the free-atmosphere lapse rate to 1 K km^{-1}. Figure 27(a) shows the obstacle shape while the vertical velocity field is illustrated in Figure 27(a), where internal waves triggered by the obstacle are clearly visible.

Appendix C. Internal gravity-wave reflectivity

In this appendix, we investigate the performance of the RDL by analyzing the internal gravity-wave reflectivity $r = E_\downarrow/E_\uparrow$, where $E_\downarrow$ and $E_\uparrow$ denote the vertical kinetic energy per unit mass (i.e. $0.5w^2$) associated with upward and downward internal gravity waves. To compute r, we use the algorithm proposed by Taylor & Sarkar (2007) which makes use of the fact that the sign of the vertical phase velocity is opposite to the sign of the vertical group velocity for internal gravity waves. Moreover, similarly to Allaerts & Meyers (2017, 2018) and Lanzilao & Meyers (2023), the upward and downward vertical kinetic energy are computed over a x-z plane including the free atmosphere only (i.e., starting at a height of 1.5 km above the capping inversion) without the buffer regions.

Results are shown in Figure 28, which illustrates the reflectivity in percentage points as a function of the ratio $\lambda_z/L_z^{\text{ra}}$. The internal gravity-wave vertical wavelength only depends upon the Brunt–Väisä frequency since the geostrophic wind is constant in our study. Therefore, the results are naturally divided into three groups defined by a free-atmosphere lapse rate of 1, 4 and 8 K/km. For the RDL to be effective, Klemp & Lilly (1977) mentioned that L_z^{ra} should be at least one time the internal gravity-wave vertical wavelength. Therefore, it is no surprise to see on average higher values of reflectivity when $\Gamma = 1$ K/km, which corresponds to a ratio $\lambda_z/L_z^{\text{ra}}$ of 1.08. As the stability of the free atmosphere increases, the ratio $\lambda_z/L_z^{\text{ra}}$ reduces to 0.38, and so does the reflectivity. Overall, r spans from a minimum of 0.41% to a maximum of 15.82%, with an average
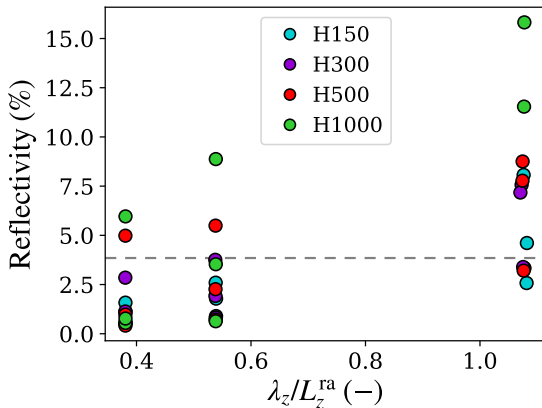
FIGURE 28. Reflectivity as a function of the ratio between the gravity-wave vertical wavelength and the RDL vertical extension.
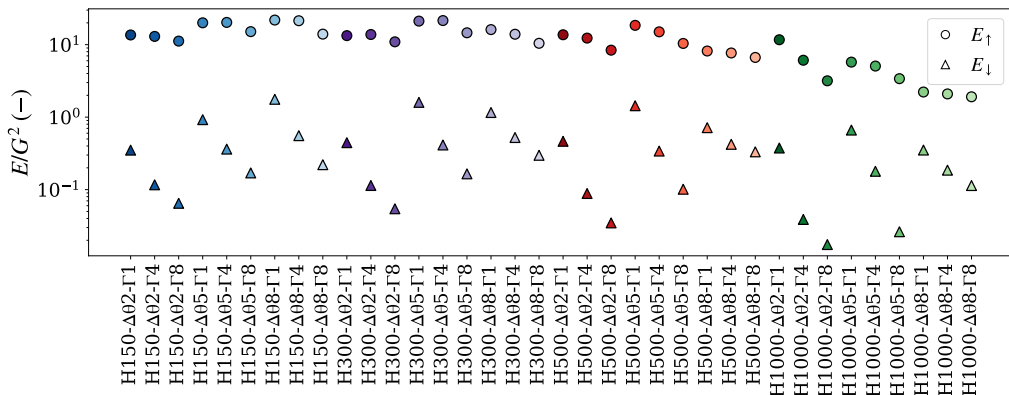

FIGURE 29. Vertical kinetic energy associated with upward ($E_\uparrow$ – circle) and downward ($E_\downarrow$ – triangle) internal waves scaled with the geostrophic wind.

value over all cases of 3.85%. The NBL reference case does not support gravity waves, therefore it is not included in the results. We note that the reflectivity values for all cases are summarized in Table 5.6.

Next, the vertical kinetic energy associated with upward and downward waves is shown in Figure 29. Overall, $E_\downarrow$ is roughly an order of magnitude lower than $E_\uparrow$. Moreover, the highest values of $E_\downarrow$ are always attained in weakly stratified atmospheres, i.e. when $\Gamma = 1$ K km^{-1}. This is expected since the RDL does not perform optimally in such a case. Finally, we note that $E_\uparrow$ gradually reduces as H increases. This is related to the fact that the capping-inversion displacement diminishes with H, therefore inducing vertical motions with lower magnitude in the free atmosphere.

REFERENCES

ABKAR, M. & PORTÉ-AGEL, F. 2013 The effect of free-atmosphere stratification on boundary-layer flow and power output from very large wind farms. *Energies* **6**, 2338–2361.

ACHESON, D.J. 1990 Elementary fluid dynamics .

ALLAERTS, D. 2016 Large-eddy simulation of wind farms in conventionally neutral and stable atmospheric boundary layers. PhD thesis, KULeuven, Leuven, Belgium.

ALLAERTS, DRIES & MEYERS, JOHAN 2015 Large eddy simulation of a large wind-turbine array in a conventionally neutral atmospheric boundary layer. *Physics of Fluids* **27** (6), 065108.

ALLAERTS, D. & MEYERS, J. 2017 Boundary-layer development and gravity waves in conventionally neutral wind farms. *J. Fluid Mech.* **814**, 95–130.

ALLAERTS, D. & MEYERS, J. 2018 Gravity waves and wind-farm efficiency in neutral and stable conditions. *Boundary-Layer Meteorol.* **166**, 269–299.

ALLAERTS, D. & MEYERS, J. 2019 Sensitivity and feedback of wind-farm induced gravity waves. *J. Fluid Mech.* **862**, 990 – 1028.

ALLAERTS, D., VANDEN BROUCKE, S., VAN LIPZIG, N. & MEYERS, J. 2018 Annual impact of wind-farm gravity waves on the belgian-dutch offshore wind-farm cluster. *J. Phys.: Conf. Ser.* **1037**, 072006.

ARCHER, CRISTINA L., MIRZAEISEFAT, SINA & LEE, SANG 2013 Quantifying the sensitivity of wind farm performance to array layout options using large-eddy simulation. *Geophysical Research Letters* **40** (18), 4963–4970, arXiv: https://agupubs.onlinelibrary.wiley.com/doi/pdf/10.1002/grl.50911.

BARTHELMIE, R. J., HANSEN, K., FRANDSEN, S. T., RATHMANN, O., SCHEPERS, J. G., SCHLEZ, W., PHILLIPS, J., RADOS, K., ZERVOS, A., POLITIS, E. S. & CHAVIAROPOULUS, P. K. 2009 Modelling and measuring flow and wind turbine wakes in large wind farms offshore. *Wind Energ.* **12**, 431–444.

BEYAZTAS, B. H., FIRUZAN, E. & BEYAZTAS, U. 2017 New block bootstrap methods: Sufficient and/or ordered. *Communications in Statistics - Simulation and Computation* **46** (5), 3942–3951, arXiv: https://doi.org/10.1080/03610918.2015.1066808.

BLEEG, J & MONTAVON, C 2022 Blockage effects in a single row of wind turbines. *Journal of Physics: Conference Series* **2265** (2), 022001.

BLEEG, J., PURCELL, M., RUISI, R. & TRAIGER, E. 2018 Wind farm blockage and the consequences of neglecting its impact on energy production. *Energies* **11**, 1609.

BON, T. & MEYERS, J. 2022 Stable channel flow with spanwise heterogeneous surface temperature. *Journal of Fluid Mechanics* **933**, A57.

BORTOLOTTI, P., TARRÉS, H. C., DYKES, K., MERZ, K., SETHURAMAN, L., VERELST, D. & ZAHLE, F. 2019 Iea wind task 37 on systems engineering in wind energy wp2.1 reference wind turbines. *Technical report* .

BOUFIDI, ELISSAVET, LAVAGNOLI, SERGIO & FONTANETO, FABRIZIO 2020 A Probabilistic Uncertainty Estimation Method for Turbulence Parameters Measured by Hot-Wire Anemometry in Short-Duration Wind Tunnels. *Journal of Engineering for Gas Turbines and Power* **142** (3), 031007, arXiv: https://asmedigitalcollection.asme.org/gasturbinespower/article-pdf/142/3/031007/6472553/gtp_142_03_031007.pdf.

BRANLARD, EMMANUEL & MEYER FORSTING, ALEXANDER R. 2020 Assessing the blockage effect of wind turbines and wind farms using an analytical vortex model. *Wind Energy* **23** (11), 2068–2086, arXiv: https://onlinelibrary.wiley.com/doi/pdf/10.1002/we.2546.

BRANLARD, EMMANUEL, QUON, ELIOT, FORSTING, ALEXANDER R. MEYER, KING, JENNIFER & MORIARTY, PATRICK 2020 Wind farm blockage effects: comparison of different engineering models. *Journal of Physics: Conference Series* **1618** (6), 062036.

CALAF, M., MENEVEAU, C. & MEYERS, J. 2010 Large eddy simulation study of fully developed wind-turbine array boundary layers. *Phys. Fluids* **22**, 015110.

CANUTO, C., HUSSAINI, M. Y., QUARTERONI, A. & ZANG, T. A. 1988 Spectral methods in fluid dynamics. *Springer-Verlag, Berlin, Germany* .

CAÑADILLAS, BEATRIZ, FOREMAN, RICHARD, STEINFELD, GERALD & ROBINSON, NICK 2023 Cumulative interactions between the global blockage and wake effects as observed by an engineering model and large-eddy simulations. *Energies* **16** (7).

CENTURELLI, G, VOLLMER, L, SCHMIDT, J, DÖRENKÄMPER, M, SCHRÖDER, M, LUKASSEN,

L J & PEINKE, J 2021 Evaluating global blockage engineering parametrizations with les. *Journal of Physics: Conference Series* **1934** (1), 012021.

CHURCHFIELD, MATTHEW, LEE, SANG, MORIARTY, PATRICK, MARTINEZ, LUIS, LEONARDI, STEFANO, VIJAYAKUMAR, GANESH & BRASSEUR, JAMES 2012 A large-eddy simulation of wind-plant aerodynamics , arXiv: https://arc.aiaa.org/doi/pdf/10.2514/6.2012-537.

CSANADY, G. T. 1974 Equilibrium theory of the planetary boundary layer with an inversion lid. *Boundary-Layer Meteorol.* **6**, 63–79.

CUSHMAN-ROISIN, B. & BECKERS, J. M. 2011 Introduction to geophysical fluid dynamics .

DELPORT, S. 2010 Optimal control of a turbulent mixing layer. PhD thesis, KULeuven, Leuven, Belgium.

DEVESSE, K., LANZILAO, L., JAMAER, S., VAN LIPZIG, N. & MEYERS, J. 2022 Extending the applicability of a wind-farm gravity-wave model to vertically non-uniform atmospheres. *Wind Energy Science Discussions* **2022**, 1–25.

DURRAN, D. R. & KLEMP, J. B. 1983 A compressible model for the simulation of moist mountain waves. *Mon. Wea. Rev.* **111**, 2341–2361.

FORNBERG, BENGT 1996 *A Practical Guide to Pseudospectral Methods*. Cambridge University Press.

GILL, A. E. 1982 Atmosphere-ocean dynamics. *International Geophysics Series* **30**, Academic Press, San Diego, USA.

GOIT, JAY PRAKASH & MEYERS, JOHAN 2013 Effect of Ekman layer on windfarm roughness and displacement height. In *Proceedings of Direct and large-eddy simulation IX, Dresden, Germany,*, pp. 423–434.

GOIT, J. P. & MEYERS, J. 2015 Optimal control of energy extraction in wind-farm boundary layers. *J. Fluid Mech.* **768**, 5–50.

HESS, G. D. 2004 The neutral, barotropic planetary bounday layer, capped by a low-level inversion. *Boundary-Layer Meteorol.* **110**, 319–355.

INOUE, M., MATHEOU, G. & TEIXEIRA, J. 2014 Les of a spatially developing atmospheric boundary layer: Application of a fringe method for the stratocumulus to shallow cumulus cloud transition. *Monthly Weather Review* **142**, 1365–1393.

KIRBY, ANDREW, NISHINO, TAKAFUMI & DUNSTAN, THOMAS D. 2022 Two-scale interaction of wake and blockage effects in large wind farms. *Journal of Fluid Mechanics* **953**, A39.

KLEMP, J. B. & LILLY, D. K. 1977 Numerical simulations of hydrostatic mountain waves. *Journal of the atmospheric sciences* **35**, 78–107.

KLEMP, J. B. & LILLY, D. R. 1975 The dynamics of wave-induced downslope winds. *Journal of Atmospheric Sciences* **32** (2), 320 – 339.

DER LAAN, M P VAN, HANSEN, K S, SØRENSEN, N N & RÉTHORÉ, P-E 2015 Predicting wind farm wake interaction with rans: an investigation of the coriolis force. *Journal of Physics: Conference Series* **625** (1), 012026.

LANGE, BERNHARD, LARSEN, SØREN, HØJSTRUP, JØRGEN & BARTHELMIE, REBECCA 2004 The influence of thermal effects on the wind speed profile of the coastal marine boundary layer. *Boundary-Layer Meteorology* **112** (3), 587–617, 048105, arXiv: https://pubs.aip.org/aip/pof/article-pdf/doi/10.1063/1.2722422/14853089/048105_1_online.pdf.

LANZILAO, LUCA & MEYERS, JOHAN 2022 Effects of self-induced gravity waves on finite wind-farm operations using a large-eddy simulation framework. *Journal of Physics: Conference Series* **2265** (2), 022043.

LANZILAO, LUCA & MEYERS, JOHAN 2023 An improved fringe-region technique for the representation of gravity waves in large eddy simulation with application to wind farms. *Boundary-Layer Meteorology* .

LIN, Y. L. 2007 *Mesoscale Dynamics*. Cambridge University Press.

LU, H. & PORTÉ-AGEL, F. 2011 Large-eddy simulation of a very large wind farm in a stable atmospheric boundary layer. *Phys. Fluids* **23**, 065101.

LUNDBLADH, A., BERLIN, S., SKOTE, M., HILDINGS, C., CHOI, J., KIM, J. & HENNINGSON, D. S. 1999 An efficient spectral method for a simulation of incompressible flow over a flat plate. *Trita-mek. Tech. Rep.: 11 KTH* .

MAAS, O. 2022 From gigawatt to multi-gigawatt wind farms: wake effects, energy budgets

and inertial gravity waves investigated by large-eddy simulations. *Wind Energy Science Discussions* **2022**, 1–31.

MAAS, OLIVER 2023 Large-eddy simulation of a 15 gw wind farm: Flow effects, energy budgets and comparison with wake models. *Frontiers in Mechanical Engineering* **9**.

MAAS, O. & RAASCH, S. 2022 Wake properties and power output of very large wind farms for different meteorological conditions and turbine spacings: a large-eddy simulation case study for the german bight. *Wind Energy Science* **7** (2), 715–739.

MASON, P. J. & THOMSON, D. J. 1992 Stochastic backscatter in large-eddy simulations of boundary layers. *Journal of Fluid Mechanics* **242**, 51–78.

MCTAVISH, SEAN, RODRIGUE, S, FESZTY, DANIEL & NITZSCHE, FRED 2015 An investigation of in-field blockage effects in closely spaced lateral wind farm configurations. *Wind Energy* **18** (11), 1989–2011.

MEDICI, D., IVANELL, S., DAHLBERG, J. A. & ALFREDSSON, P. H. 2011 The upstream flow of a wind turbine: blockage effect. *Wind Energy* **14** (5), 691–697, arXiv: https://onlinelibrary.wiley.com/doi/pdf/10.1002/we.451.

MEYER FORSTING, ALEXANDER RAUL, TROLDBORG, NIELS & GAUNAA, MAC 2017 The flow upstream of a row of aligned wind turbine rotors and its effect on power production. *Wind Energy* **20** (1), 63–77.

MEYERS, J. & MENEVEAU, C. 2010 Large eddy simulations of large wind-turbine arrays in the atmospheric boundary layer. *48th AIAA Aerospace Sciences Meeting* .

MEYERS, JOHAN & SAGAUT, PIERRE 2007 Is plane-channel flow a friendly case for the testing of large-eddy simulation subgrid-scale models? *Physics of Fluids* **19** (4), 048105, arXiv: https://pubs.aip.org/aip/pof/article-pdf/doi/10.1063/1.2722422/14853089/048105_1_online.pdf.

MOENG, C. H. 1984 A large-eddy-simulation model for the study of the planetary boundary-layer turbulence. *Journal of the atmospheric science* **41**, 2052–2062.

MUNTERS, WIM, MENEVEAU, CHARLES & MEYERS, JOHAN 2016 Shifted periodic boundary conditions for simulations of wall-bounded turbulent flows. *Physics of Fluids* **28** (2), 025112.

MUNTERS, W. & MEYERS, J. 2018 Dynamic strategies for yaw and induction control of wind farms based on large-eddy simulation and optimization. *Energies* **11**, 177.

NAPPO, C. J. 2002 An introduction to atmospheric gravity waves. *International Geophysics Series* **85**, Academic Press, Waltham, USA.

NORDSTROM, J., NORDIN, N. & HENNINGSON, D. 1999 The fringe region technique and the fourier method used in the direct numerical simulation of spatially evolving viscous flows. *SIAM J. Sci. Comput.* **20**, 1365–1393.

OTTE, MARTIN J. & WYNGAARD, JOHN C. 2001 Stably stratified interfacial-layer turbulence from large-eddy simulation. *Journal of Atmospheric Sciences* **58** (22), 3424–3442.

PEDERSEN, JESPER G., GRYNING, SVEN-ERIK & KELLY, MARK 2014 On the structure and adjustment of inversion-capped neutral atmospheric boundary-layer flows: Large-eddy simulation study. *Boundary-Layer Meteorology* **153**, 43–62.

PORTÉ-AGEL, F., BASTANKHAH, M. & SHAMSODDIN, S. 2020 Wind-turbine and wind-farm flows: A review. *Boundary-Layer Meteorol* **174**, 1–59.

PORTÉ-AGEL, F., WU, Y. T. & CHEN, C. H. 2013 A numerical study of the effects of wind direction on turbine wakes and power losses in a large wind farm. *J. Energies* **6 (10)**, 5297–5313.

RAMPANELLI, G. & ZARDI, D. 2004 A method to determine the capping inversion of the convective boundary layer. *J. Appl. Meteor.* **43**, 925–933.

SACHSPERGER, JOHANNES, SERAFIN, STEFANO & GRUBIŠIĆ, VANDA 2015 Lee waves on the boundary-layer inversion and their dependence on free-atmospheric stability. *Frontiers in Earth Science* **3**.

SANCHEZ GOMEZ, M., LUNDQUIST, J. K., MIROCHA, J. D. & ARTHUR, R. S. 2023 Investigating the physical mechanisms that modify wind plant blockage in stable boundary layers. *Wind Energy Science Discussions* **2023**, 1–28.

SCHLATTER, P., ADAMS, N. & KLEISER, L. 2005 A windowing method for periodic inflow/outflow boundary treatment of non-periodic flows. *Journal of Computational Physics* **206**, 505–535.

SCHNEEMANN, J., THEUER, F., ROTT, A., DÖRENKÄMPER, M. & KÜHN, M. 2021 Offshore wind farm global blockage measured with scanning lidar. *Wind Energy Science* **6**, 521–538.

SEGALINI, A. 2021 An analytical model of wind-farm blockage. *Journal of Renewable and Sustainable Energy* **13** (3), 033307, arXiv: https://doi.org/10.1063/5.0046680.

SEGALINI, A. & DAHLBERG, J. A. 2019 Blockage effects in wind farms. *Wind Energy* **23(2)**, 120–128.

SMEDMAN, A.S., BERGSTROM, H. & GRISOGONO, B. 1997 Evolution of stable internal boundary layers over a cold sea. *Journal of Geophysical Research* **102**, 1091–1099.

SMITH, R. 2023 The wind farm pressure field. *Wind Energy Science Discussions* **2023**, 1–14.

SMITH, R. B. 2010 Gravity wave effects on wind farm efficiency. *Wind Energy* **13**, 449–458.

SMITH, RONALD B. 2022 A linear theory of wind farm efficiency and interaction. *Journal of the Atmospheric Sciences* .

SPALART, P. R. & WATMUFF, J. H. 1993 Experimental and numerical study of a turbulent boundary layer with pressure gradients. *J. Fluid Mech.* **249**, 337–371.

SPIEGEL, E.A. & VERONIS, G. 1960 On the boussinesq approximation for a compressible fluid. *apj* **131**, 442.

STEVENS, B., MOENG, C. H. & SULLIVAN, P. P. 2000 Entrainment and subgrid length scales in large-eddy simulations of atmospheric boundary-layer flows. *Symposium on Developments in Geophysical Turbulence* **58**, 253–269.

STEVENS, RICHARD J.A.M., GAYME, DENNICE F. & MENEVEAU, CHARLES 2016 Effects of turbine spacing on the power output of extended wind-farms. *Wind Energy* **19** (2), 359–370, arXiv: https://onlinelibrary.wiley.com/doi/pdf/10.1002/we.1835.

STEVENS, R. J. A. M., GAYME, D. F. & MENEVEAU, C. 2014*a* Large eddy simulation studies of the effects of alignment and wind farm length. *Phys. Fluids* **6**, 023105.

STEVENS, R. J. A. M., GRAHAM, J. & MENEVEAU, C. 2014*b* A concurrent precursor inflow method for large eddy simulations and applications to finite length wind farms. *Renewable Energy* **68**, 46–50.

STIEREN, ANJA & STEVENS, RICHARD J.A.M. 2022 Impact of wind farm wakes on flow structures in and around downstream wind farms. *Flow* **2**, E21.

STRICKLAND, JESSICA M.I. & STEVENS, RICHARD J.A.M. 2022 Investigating wind farm blockage in a neutral boundary layer using large-eddy simulations. *European Journal of Mechanics - B/Fluids* **95**, 303–314.

STRICKLAND, J. M. I. & STEVENS, R. J. A. M. 2020 Effect of thrust coefficient on the flow blockage effects in closely-spaced spanwise-infinite turbine arrays. *Journal of Physics: Conference Series* **1618** (6), 062069.

SUTHERLAND, B. R. 2010 Internal gravity waves. *Cambridge University Press.* .

TAYLOR, J. R. & SARKAR, S. 2007 Internal gravity waves generated by a turbulent bottom ekman layer. *J. Fluid Mech.* **590**, 331–354.

TAYLOR, J. R. & SARKAR, S. 2008 Direct and large eddy simulations of a bottom ekman layer under an external stratification. *Int. J. Heat Fluid Flow* **29**, 721–732.

TAYLOR, P. K. & YELLAND, M. J. 2000 The dependence of sea surface roughness on the height and steepness of the waves. *Journal of Physical Oceanography* **31**.

TEIXEIRA, M. A. C. 2014 The physics of orographic gravity wave drag. *Frontier in Physics* **2**.

TÜRK, MATTHIAS & EMEIS, STEFAN 2010 The dependence of offshore turbulence intensity on wind speed. *Journal of Wind Engineering and Industrial Aerodynamics* **98** (8), 466–471.

VERSTAPPEN, R. W. C. P. & VELDMAN, A. E. P. 2003 Symmetry-preserving discretization of turbulent flow. *Journal of Computational Physics* **187**, 343–368.

VOSPER, S. B. 2004 Inversion effects on mountain lee waves. *Quarterly Journal of the Royal Meteorological Society* **130** (600), 1723–1748, arXiv: https://rmets.onlinelibrary.wiley.com/doi/pdf/10.1256/qj.03.63.

WU, K. L. & PORTÉ-AGEL, F. 2017 Flow adjustment inside and around large finite-size wind farms. *Energies* **10**, 2164.

WU, YU-TING, LIAO, TEH-LU, CHEN, CHANG-KUO, LIN, CHUAN-YAO & CHEN, PO-WEI 2019 Power output efficiency in large wind farms with different hub heights and configurations. *Renewable Energy* **132**, 941–949.

WU, YU-TING & PORTÉ-AGEL, FERNANDO 2011 Large-eddy simulation of wind-turbine wakes: Evaluation of turbine parametrisations. *Springer* **138**, 345–366.

Wu, Y.-T. & Porté-Agel, F. 2013 Simulation of turbulent flow inside and above wind farms: model validation and layout effects. *Boundary-Layer Meteorol.* **146 (2)**, 181–205.

Wu, Y. T. & Porté-Agel, F. 2015 Modeling turbine wakes and power losses within a wind farm using les: An application to the horns rev offshore wind farm. *Renewable Energy* **75**, 945–955.

Wyngaard, John C. 2010 *Turbulence in the Atmosphere*. Cambridge University Press.

Yang, D., Meneveau, C. & Shen, L. 2014*a* Effect of downwind swells on offshore wind energy harvesting – a large-eddy simulation study. *Renewable Energy* **70**, 11–23, special issue on aerodynamics of offshore wind energy systems and wakes.

Yang, D., Meneveau, C. & Shen, L. 2014*b* Large-eddy simulation of offshore wind farm. *Phys. Fluids* **26**, 025101.

Zilitinkevich, S. & Esau, I. 2003 The effect of baroclinicity on the equilibrium depth of neutral and stable planetary boundary layers. *Quarterly Journal of the Royal Meteorological Society* **129**.

Zilitinkevich, Sergej, Esau, Igor & Baklanov, Alexander 2007 Further comments on the equilibrium height of neutral and stable planetary boundary layers. *Quarterly Journal of the Royal Meteorological Society* **133** (622), 265–271, arXiv: https://rmets.onlinelibrary.wiley.com/doi/pdf/10.1002/qj.27.

Zilitinkevich, S. S. 1989 Velocity profiles, the resistance law and the dissipation rate of mean flow kinetic energy in a neutrally and stably stratified planetary boundary layer. *Boundary-Layer Meteorol.* **46**, 367–387.

Zilitinkevich, S. S. & Esau, I. N. 2002 On integral measures of the neutral barotropic planetary boundary layer. *Boundary-Layer Meteorology* **104**, 371–379.

Zilitinkevich, Sergej S. & Esau, Igor N. 2005 Resistance and heat-transfer laws for stable and neutral planetary boundary layers: Old theory advanced and re-evaluated. *Quarterly Journal of the Royal Meteorological Society* **131** (609), 1863–1892, arXiv: https://rmets.onlinelibrary.wiley.com/doi/pdf/10.1256/qj.04.143.